

PAPER • OPEN ACCESS

Overview of interpretive modelling of fusion performance in JET DTE2 discharges with TRANSP




























To cite this article: Ž. Štancar *et al* 2023 *Nucl. Fusion* **63** 126058

View the [article online](#) for updates and enhancements.

You may also like

- [Peripheral temperature gradient screening of high-Z impurities in optimised 'hybrid' scenario H-mode plasmas in JET-ILW](#)
A.R. Field, F.J. Casson, D. Fajardo et al.
- [Tungsten transport in JET H-mode plasmas in hybrid scenario, experimental observations and modelling](#)
C. Angioni, P. Mantica, T. Pütterich et al.
- [Validation of D–T fusion power prediction capability against 2021 JET D–T experiments](#)
Hyun-Tae Kim, Fulvio Auriemma, Jorge Ferreira et al.

Overview of interpretive modelling of fusion performance in JET DTE2 discharges with TRANSP

Ž. Štancar^{1,*} , K.K. Kirov¹ , F. Auriemma^{2,13} , H.-T. Kim¹ , M. Poradziński¹ , R. Sharma¹, R. Lorenzini² , Z. Ghani¹, M. Gorelenkova³ , F. Poli³ , A. Boboc¹ , S. Brezinsek⁴ , P. Carvalho¹, F.J. Casson¹ , C.D. Challis¹, E. Delabie⁵, D. Van Eester⁶ , M. Fitzgerald¹, J.M. Fontdecaba⁷ , D. Gallart⁸ , J. Garcia⁹ , L. Garzotti¹ , C. Giroud¹, A. Kappatou¹⁰ , Ye.O. Kazakov⁶, D.B. King¹, V.G. Kiptily¹ , D. Kos¹ , E. Lerche^{1,6}, E. Litherland-Smith¹, C.F. Maggi¹ , P. Mantica¹¹ , M.J. Mantsinen^{8,14}, M. Maslov¹ , S. Menmuir¹, M. Nocente¹² , H.J.C. Oliver¹ , S.E. Sharapov¹ , P. Sirén¹, E.R. Solano⁷ , H.J. Sun¹ , G. Szepesi¹ and JET Contributors^{a,b}

¹ United Kingdom Atomic Energy Authority, Culham Science Centre, Abingdon, United Kingdom of Great Britain and Northern Ireland

² Consorzio RFX (CNR, ENEA, INFN, Università di Padova, Acciaierie Venete SpA), Padova, Italy

³ Princeton Plasma Physics Laboratory, Princeton, NJ, United States of America

⁴ Forschungszentrum Jülich, Institut für Energie und Klimaforschung–Plasmasphysik, Jülich, Germany

⁵ Oak Ridge National Laboratory, Oak Ridge, TN, United States of America

⁶ Laboratory for Plasma Physics, Ecole Royale Militaire, Brussels, Belgium

⁷ Laboratorio Nacional de Fusión, CIEMAT, Madrid, Spain

⁸ Barcelona Supercomputing Center, Barcelona, Spain

⁹ CEA, IRFM, Saint-Paul-lez-Durance, France

¹⁰ Max-Planck-Institut für Plasmaphysik, Garching, Germany

¹¹ Institute for Plasma Science and Technology, CNR, Milano, Italy

¹² Dipartimento di Fisica ‘G. Occhialini’, Università di Milano-Bicocca, Milan, Italy

¹³ Istituto per la Scienza e la Tecnologia dei Plasmi del CNR, Padova, Italy

¹⁴ ICREA, Barcelona, Spain

E-mail: ziga.stancar@ukaea.uk

Received 30 August 2023

Accepted for publication 13 October 2023

Published 6 November 2023



CrossMark

Abstract

In the paper we present an overview of interpretive modelling of a database of JET-ILW 2021 D-T discharges using the TRANSP code. The main aim is to assess our capability of computationally reproducing the fusion performance of various D-T plasma scenarios using different external heating and D-T mixtures, and to understand the performance driving mechanisms. We find that interpretive simulations confirm a general power-law relationship between increasing external heating power and fusion output, which is supported by absolutely

^a See the author list of ‘Overview of T and D-T results in JET with ITER-like wall’ by Maggi *et al* to be published in Nuclear Fusion Special Issue: Overview and Summary Papers from the 29th Fusion Energy Conference (London, UK, 16–21 October 2023).

^b See Mailloux *et al* 2022 (<https://doi.org/10.1088/1741-4326/ac47b4>) for JET Contributors.

* Author to whom any correspondence should be addressed.



Original Content from this work may be used under the terms of the [Creative Commons Attribution 4.0 licence](https://creativecommons.org/licenses/by/4.0/). Any further distribution of this work must maintain attribution to the author(s) and the title of the work, journal citation and DOI.

calibrated neutron yield measurements. A comparison of measured and computed D-T neutron rates shows that the calculations' discrepancy depends on the absolute neutron yield. The calculations are found to agree well with measurements for higher performing discharges with external heating power above ~ 20 MW, while low-neutron shots display an average discrepancy of around $+40\%$ compared to measured neutron yields. A similar trend is found for the ratio between thermal and beam-target fusion, where larger discrepancies are seen in shots with dominant beam-driven performance. We compare the observations to studies of JET-ILW D discharges, to find that on average the fusion performance is well modelled over a range of heating power, although an increased unsystematic deviation for lower-performing shots is observed. The ratio between thermal and beam-induced D-T fusion is found to be increasing weakly with growing external heating power, with a maximum value of $\gtrsim 1$ achieved in a baseline scenario experiment. An evaluation of the fusion power computational uncertainty shows a strong dependence on the plasma scenario type and fusion drive characteristics, varying between $\pm 25\%$ and 35% . D-T fusion alpha simulations show that the ratio between volume-integrated electron and ion heating from alphas is $\lesssim 10$ for the majority of analysed discharges. Alphas are computed to contribute between $\sim 15\%$ and 40% to the total electron heating in the core of highest performing D-T discharges. An alternative workflow to TRANSP was employed to model JET D-T plasmas with the highest fusion yield and dominant non-thermal fusion component because of the use of fundamental radio-frequency heating of a large minority in the scenario, which is calculated to have provided $\sim 10\%$ to the total fusion power.

Keywords: deuterium-tritium plasma, integrated modelling, fusion performance, JET, TRANSP

(Some figures may appear in colour only in the online journal)

1. Introduction

Fusion power measurements are an essential tokamak operational parameter from the perspective of safety as well as tracking progress towards achieving burning plasma conditions. It is therefore important to develop and validate integrated modelling tools capable of interpreting the fusion performance of current experiments, and making accurate predictions in ITER-like conditions and those expected in pilot fusion plants. A range of plasma scenarios with varying fusion performance was tested in JET's 2021 deuterium-tritium campaign (DTE2) with the ITER-like-wall (ILW, metal Be/W), which provided a unique opportunity to benchmark interpretive plasma modelling codes in reactor relevant conditions.

In this paper we present an overview of interpretive modelling of over 80 JET ILW DTE2 discharges using the TRANSP code [1–3]. The main aim is to analyse our capability of reproducing the fusion performance of various D-T plasma scenarios, in which different external heating and D-T mixture configurations were used in an effort to maximize the fusion energy output. We summarize the main motivation for this work in the following points:

- (i) JET has the unique capability to measure time-dependent absolute fusion power produced in D-T plasmas due to its absolutely calibrated 14 MeV neutron detectors [4, 5]. In the calibration procedure a D-T neutron generator is moved through the vacuum vessel with the help of a remote handling system in a series of about 200 toroidal and poloidal positions. In the process the response and spatial sensitivity of three independent fission chambers

and the neutron activation system to a 14 MeV neutron source is measured. It is the neutron activation system that is absolutely validated in the calibration procedure due to its proximity to the plasma source, while the fission chambers are cross-calibrated against it. The complex and state-of-the-art procedure, which requires detailed neutron transport computational support and dedicated plasma calibration discharges, has a total uncertainty below $\sim 10\%$ and is planned to be applied to ITER [6–9]. In this work we exploit the absolute neutron yield measurements obtained in DTE2 to benchmark state-of-the-art plasma code calculations, and provide a foundation to validate and tune predictive models. This enables the development of multi-physics whole-device workflows and synthetic diagnostics models, facilitating reliable fusion performance extrapolations for ITER and future fusion devices [10, 11].

- (ii) Previous interpretive modelling work aimed at reproducing JET's fusion performance in D and D-T plasmas achieved various degrees of agreement between calculations and measurements. Most notably a general over-prediction of the computed neutron yield was observed over a range of studies with codes such as TRANSP and ASCOT [12–18]. A comprehensive analysis of JET D plasma performance with a carbon wall is presented in [12], where it is found that the calculations overestimate the measured neutron rates by up to 50% , independently of fusion performance or its drivers. The cause of the observed 'neutron deficit' is investigated through uncertainties in fuel dilution, equilibrium mapping errors, neutral beam injection (NBI) power and penetration, as

well as broadband and magnetohydrodynamic (MHD) transport. No single mechanism was found to explain the observations, while it was postulated that an unfavourable combination of systematic modelling errors might play a role. The study published in [13] looks at JET's trace tritium experiments in which a T beam was injected into a pure D plasma. Similarly, the study had observed an overestimation of the computed fusion power for both the D-D and D-T neutron dominated phases, which was pronounced in higher density plasmas. In order to obtain a match in the neutron rates the authors artificially applied a reduction in T-NBI power of up to 40% and a fast ion anomalous diffusion between 5 and 10 m² s⁻¹. These are large values both for the expected uncertainty in beam power, as well as observed anomalous transport. Additionally no effect of the growth of low n/m MHD modes on the neutron yield was found. The remaining studies listed above focus on analysing the neutron yield in JET's 1997 D-T campaign (DTE1) [19] or JET-ILW deuterium experiments, and observe an improvement in computational agreement for higher performing discharges. In summary, an unambiguous explanation for the discrepancies between measured and computed fusion power has not been identified in preceding work, with suspected contributing causes varying from systematic experimental uncertainties in input data to unaccounted fast ion turbulent transport. In this paper we revisit the fusion power comparison through a large database of JET-ILW D and D-T plasma TRANSP runs. The discharges' plasma parameters cover a wide range of plasma current, B-field, electron density, electron and ion temperature, external heating power, etc values—resulting in variations of neutron yields over several orders of magnitude. Additionally an improved modelling workflow has been adopted, which facilitates modelling consistency and evaluation of systematic input uncertainty.

- (iii) An important physics outcome of JET's DTE2 experiment is the insight into alpha particle physics, e.g. to understand the role alphas play in plasma self-heating, and driving plasma instabilities such as Alfvén eigenmodes. Because the alpha particle source is linearly proportional to the neutron yield, the fidelity of alpha particle effects modelling is related to our capability to reproduce the fusion performance. In the paper we present an overview of the calculated trends of alpha power flow into the electron and ion channels, and assess the alpha pressure and power in comparison with the fast NBI ions.
- (iv) Probing the readiness of interpretive capabilities of TRANSP for analyses of D-T fusion performance, we find that the best performing pulses in the DTE2 campaign, the hybrid-like T-rich scenario highly driven by beam-target fusion, cannot be modelled fully with default TRANSP capabilities. Namely in this scenario the fundamental D radio-frequency (RF) heating of a large minority is applied—while the evolution of the resulting fast deuterium ions can be performed in TRANSP with the Fokker-Planck Program (FPP) code, this is not communicated to the fusion reactivity calculator—adopting an alternative

modelling workflow, we assess the additional contribution to the total fusion output.

- (v) New deuterium-tritium plasma results have been produced in JET's DTE2 campaign more than 20 years after DTE1 [19]. In this time significant progress has been made in the understanding of tokamak physics, development of plasma modelling workflows, and improvement of JET's diagnostics systems [20, 21]. Throughout the paper we showcase the effect of these joint improvements on integrated modelling, discuss advancements in diagnostics analysis and code fidelity, and address the modelling challenges encountered.

The paper is structured as follows: in section 2 the modelling workflow is presented, emphasizing the importance of consistent preparation of input data and equilibrium reconstruction. We describe the modelling tools used, detail which diagnostics are used for the preparation of input and their fits, and showcase how these are validated. We describe the JET-ILW DTE2 and D campaign discharge databases, followed by a display of the regular consistency checks for the DTE2 dataset, i.e. agreement between measurements and synthetic TRANSP signals for integrated electron density, plasma stored energy, neutron yield, and D-T fuel mixture. In section 3 we delve deeper into the analysis of fusion power calculations, which is split into several sub-sections: section 3.1 describes fusion reactivity drivers for a selection of plasma scenarios, which we tie to the relationship between thermal and beam-target fusion contributions. We elaborate on the role of NBI and RF heating, and the effects these have on the electron and ion power balance, in addition to beam density peaking in D-T, T_i/T_e , plasma rotation, and effective collisionality. In section 3.2 we discuss the excellent match between DTE2 measurements and simulations for high performance discharges, and the over-prediction observed for lower-performing ones. We compare the findings to the results from JET-ILW deuterium campaigns, and discuss potential reasons for the observed discrepancies; section 3.3 delves into uncertainties of D-T relevant quantities—we chose three discharges from the low- and high-power branch (NBI-only neutron calibration discharge #99812, baseline #99863, and hybrid #99950) and vary parameters such as the D-T fuel ratio, n_e , T_e , T_i , within their respective uncertainties and produce a computational uncertainty assessment; section 3.4 discusses the observation from fusion alpha modelling, focusing on the trends of alpha heating of electrons and ions, as well as the alpha pressure. In section 4 we describe the modelling challenges we have encountered in DTE2 with TRANSP and its heating modules. We will study one of the T-rich fusion energy record shots #99972, in which the fundamental RF heating of a thermal D population is expected to contribute up to ~15% to the total neutron rate, which is not computed in TRANSP by default. We will showcase how we evolve the D-RF tail with a Fokker-Planck solver and use this distribution function to calculate the additional D-T fusion rate. In section 5, the discussion and conclusions section, the highlight findings of the project are presented, together with a description of future work and modelling suggestions, especially from the perspective of

improving the fusion power match for low-power discharges. We comment on how the reference interpretive runs will be used in further studies.

2. Integrated modelling workflow

2.1. TRANSP database

The results presented in the following chapters are based on data obtained during the JET-ILW D (C38 in 2018–2020) [22] and DTE2 (C41 in 2021) campaigns [23]. The database of interpretive runs comprises 79 deuterium discharges (with some discharges including a ^1H or ^3He second thermal species with concentrations larger than that of a typical RF minority, i.e. $\gtrsim 5\%$) and 87 deuterium-tritium discharges (with varying ratios of D-T fuel mixture). Both databases include a variety of plasma scenarios—from the perspective of fusion performance the chosen scenarios purposely exhibit large variations in fusion power and differ in the mechanisms driving the performance. The criteria for selecting which discharges to model were mainly the availability of validated diagnostics data and the scientific relevance of the experiment. Generally it is the higher performing discharges that have been designed and optimized to sustain and maximize fusion power, while the lower performing shots are aimed at studying specific plasma physics phenomena with little need for high fusion output. In the analysis we exploit the broad range of shot characteristics to identify fusion performance and computational fidelity trends. Throughout the paper we adopt a discharge notation based on the scenario type, described in detail in the bullets below:

- **Baseline:** 50-50 D-T, ELMy (not type I) H-mode scenario generally performed at high toroidal current $I_p \geq 3.0$ MA, toroidal field $B_t \sim 3.3$ T, safety factor of $q_0 < 1$ and $q_{95} \sim 3$, beta values of $\beta_p < 1$ and $\beta_N \sim 1.8$ – 2.0 , high electron density (core line-averaged density $\gtrsim 7.5 \cdot 10^{19} \text{ m}^{-3}$), mixed 50-50 D-T NBI and H RF minority heating, D pellet ELM-pacing, aimed at maximizing thermal fusion performance [20, 24, 25];
- **Hybrid:** 50-50 D-T, Type I ELMy H-mode scenario generally performed at lower current than baseline with $2.2 \leq I_p \leq 2.5$ MA, toroidal field $B_t \sim 3.45$ T, shaped broad q-profile at $q_0 \geq 1$ and $4.5 \leq q_{95} \leq 5.0$, beta values of $\beta_p \geq 1$ and $\beta_N \sim 2.0$ – 2.3 , modest electron density (core line-averaged density within $4.0 \times 10^{19} \lesssim \bar{n}_e \lesssim 5.5 \times 10^{19} \text{ m}^{-3}$), mixed 50-50 D-T NBI and H RF minority heating, aimed at improved stability and reduced core transport for better confinement [26–28];
- **T-rich:** hybrid-like H-mode scenario optimized to maximize non-thermal fusion with a D-T fuel mix of $\sim 15\%$ – 85% , single species D NBI and fundamental D RF heating with T gas injection—achieved fusion energy record in DTE2 [29, 30];
- **Energetic particle afterglow (EP):** 50-50 D-T H-mode discharges with mixed D-T NBI-only heating with two reference plasmas—ITB lowest density discharges for high transient fusion power, exploiting q^2 scaling in TAE stability,

- performed at toroidal current $I_p = 2.9$ MA, toroidal field $B_t = 3.45$ T, elevated q-profile with $q_0 > 1.5$, $q_{95} = 3.8$ and conventional magnetic shear, with $\beta_N \sim 1.3$ and $T_i \gg 2T_e$. Hybrid-like scenario with highest transient fusion power, exploiting β_α scaling in TAE stability, performed at toroidal current $I_p = 2.3$ MA, toroidal field $B_t = 3.45$ T, with $\beta_N \sim 2$. Scenario aimed at facilitating conditions for measurement of alpha heating and alpha driven effects [31, 32];
- **RF heating (RF):** mostly hybrid-like H-mode discharges at modest toroidal current $I_p \sim 2.5$ MA and varying toroidal field, testing different RF heating schemes in JET D-T with Be/W wall, envisaged for ITER D-T operation, e.g. second harmonic D majority, second harmonic T majority, and ^3He minority [33–36];
- **Seeded:** 50-50 D-T, neon-seeded ELMy H-mode performed at high triangularity with strike points on vertical target, at $I_p = 2.5$ MA, toroidal field of $B_t = 2.8$ T, safety factor of $q_0 < 1$ and $q_{95} = 3.2$, beta values of $\beta_p < 1$ and $\beta_N \sim 1.2$ – 2 , high electron density (core line-averaged density $\gtrsim 7.5 \times 10^{19} \text{ m}^{-3}$), mixed D-T NBI and H RF minority heating, aimed at assessing for the first time the core-edge integration of an ELMy H-mode in D-T with a Be/W wall and a partially detached divertor [37, 38];
- **Calibration:** 50-50 D-T H-mode discharges with mixed D-T NBI-only heating, performed at a toroidal current of $I_p = 2.0$ MA and toroidal field of $B_t = 2.4$ T, aimed at cross-calibrating the neutron yield monitors against foil activation measurements, performed with the neutron activation system. The neutron calibration discharges were chosen as representatives of low-power shots, typically run for specific transport and confinement physics studies, exhibiting similar operational parameters and fusion performance drivers.
- **Other:** mixed discharge types that are not directly addressed in the paper, and were predominantly performed at lower density (core line-averaged density $\lesssim 4 \times 10^{19} \text{ m}^{-3}$), current, and heating power with varying D-T composition, and include both L-mode and H-mode discharges.

All the discharges were modelled interpretively with TRANSP and its coupled heating modules—the NUBEAM orbit tracking code for beam injected ions and alpha particle tracking [39], and TORIC RF wave solver [40]. The integrated modelling framework OMFIT was used for orchestrating the input data preparation and analysis of the modelling results [41, 42]. The NBI + RF synergistic effects, important for example in discharges with 2nd harmonic RF acceleration of fast NBI ions, were modelled with the quasi-linear RF kick operator [43, 44]. The operator communicates TORIC computed RF electric field components and perpendicular wave vectors for each toroidal mode to NUBEAM [45].

2.2. Input data preparation

In order for individual simulations to be comparable and enable a cross-scenario analysis, the input data preparation workflow was pre-defined, followed by data consistency checks. The interpretive analyses used fitted electron density and temperature profiles as input—fits for both quantities were

done with high resolution Thomson scattering (HRTS) [46] and LIDAR (core n_e) [47] data, with the temperature additionally constrained by electron cyclotron emission data [48] (covering core and edge regions). Thomson scattering n_e measurements are cross-calibrated against the absolutely calibrated interferometer line-integrated density. Because this is done in discharges' ohmic phase a discrepancy between HRTS and interferometer measurements can be observed in the heating phase of H-mode plasmas, which has been found to increase proportionally to T_e . Various possible reasons for this discrepancy have been studied such as the effects of background plasma light, laser polarization, signal to noise ratio in the raw data, and EFIT equilibrium reconstruction, however it is not yet fully understood [49]. The discrepancy is corrected by applying a scalar scaling to the HRTS measurements, derived from their deviation from multiple interferometer lines-of-sight, covering both edge and core plasma. The correction factor is time-dependent, constant over the radius, and on average varies between $1.0 \sim 0.9$. The correction is found to vary little within individual discharges' modelling intervals, and generally becomes larger with increasing external heating power. The ion temperature and rotation were prescribed based on fits from core and edge charge-exchange recombination spectroscopy (CXRS) diagnostics [50–52]—while these measurements were generally of good quality with the carbon wall, the inherent CX conditions are less favourable in the Be/W wall, which prompted an upgrade of the core CXRS diagnostics specifically for DTE2. Diagnostic neon puffing is commonly used to enable core CXRS measurements from the Ne X CX spectrum, but measurements in the core are still strongly affected by the diffusion of Ne gas from the edge, which is dependent on the plasma density. It is therefore not uncommon for the quality of the CX signal to be poorer close to the magnetic axis, i.e. $\rho \lesssim 0.3$, which can strongly affect the calculation of the total fusion rate. To better constrain T_i and plasma rotation fits in the core, high-resolution crystal x-ray spectrometer measurements are used [53], in addition to surrogate points obtained through steady-state electron-ion power balance calculations [54], used mainly to ensure that the core T_i fits lie within the estimate of maximum sustainable temperature difference between ions and electrons. In general the profiles were fitted with a combination of polynomial (core) and modified hyperbolic tangent (edge) functions for H-mode plasmas, and cubic splines for L-mode plasmas. The fit uncertainty was calculated as the combination of two uncorrelated uncertainties, namely the deviation of the fit from the available measurement constraints, and the uncertainty of the measurements. In average the former were below 5%, while the measurements uncertainty varied between 5% and 10%, which yields an approximate 1σ fit uncertainty of $\sim 10\%$.

The equilibrium and safety factor were taken from an EFIT++ time-evolved reconstruction constrained by an improved magnetics measurements suite and pressure profiles, i.e. including kinetic profile fits and NBI/RF accelerated fast ions, as well as MHD markers and polarimetry measurements [55]. The equilibrium was applied to kinetic profile data mapping and was fully prescribed in TRANSP, i.e. an internal solver was not used. In order to obtain a

converged equilibrium solution an iterative approach was adopted, starting with a magnetics-only reconstruction, which was fed into TRANSP to obtain an improved plasma pressure profile. This was followed by consecutive steps including mapping, executing TRANSP, and EFIT++ reconstructions, until a close match was reached with the preceding iteration (two iterations were generally sufficient). Through this improved equilibrium reconstruction method we observed a consistent match between the equilibrium-computed boundary location and the one inferred by density and temperature edge measurements, as well as agreement between the EFIT++ and TRANSP calculated plasma stored energy. In contrast, the use of more rudimentary EFIT reconstruction methods resulted in the need to radially shift density and temperature profiles to obtain reasonable separatrix values, and led to a systematic mismatch in the stored energy calculated in the reconstruction and modelling codes. An example of an embedded fit consistency check for the baseline discharge #99863 is shown in figure 1, where the electron density, electron temperature, ion temperature and toroidal rotation fits are compared against diagnostics measurements described above. In panel (c) of figure 1 one can observe that the T_i CX measurements closest to the axis, at $\rho \sim 0.25$, have values below the expected fit trend—this is due to the low CX signal intensity discussed above, albeit there was Ne injected. A T_i surrogate estimate derived from power balance constraints (red circle) and a high-resolution crystal x-ray spectrometer measurements (magenta circle) were used as additional core constraints. The CXRS measurements are divided into four diagnostics groups with two denoting core measurements (green and orange), and two edge measurements (blue and cyan). If available, CX data with cross section and fine-structure corrections was used [56].

The deuterium-tritium plasma composition was prescribed based on measurements of relative H+D+T hydrogenic species concentrations by the residual gas analysis diagnostics, located in the sub-divertor plenum [57]. Since this is an edge measurement the D-T fuel mixture has to be extrapolated to the core, which was done by including impurity and beam dilution corrections. The beam dilution correction requires an iterative approach, because it is based on a beam density calculation stemming from a converged slowing-down solution. This means that the core D-T ratio in the first run is computed using a prescribed surrogate beam dilution profile with a beam concentration estimate of $\sim 5\%$ with respect to n_e . In the following simulation's D-T composition extrapolation, the NUBEAM computed beam density profile is available (two iterations were generally sufficient). It was found that the computed core value of D/T concentration coincided closely with the edge value, which is addressed in more detail in 3.3. The fuel mix concentrations were cross-checked against an independent measurement by divertor optical gas spectroscopy [58]. The concentration of the RF minority was prescribed based on residual gas analysis as a fixed fraction of the electron density, with an average value between 2.5% and 5.0%, with protium being the most common RF species and individual discharges employing ^3He for physics studies. Through a combined analysis of the effective charge, soft x-ray, bolometry, and CXRS

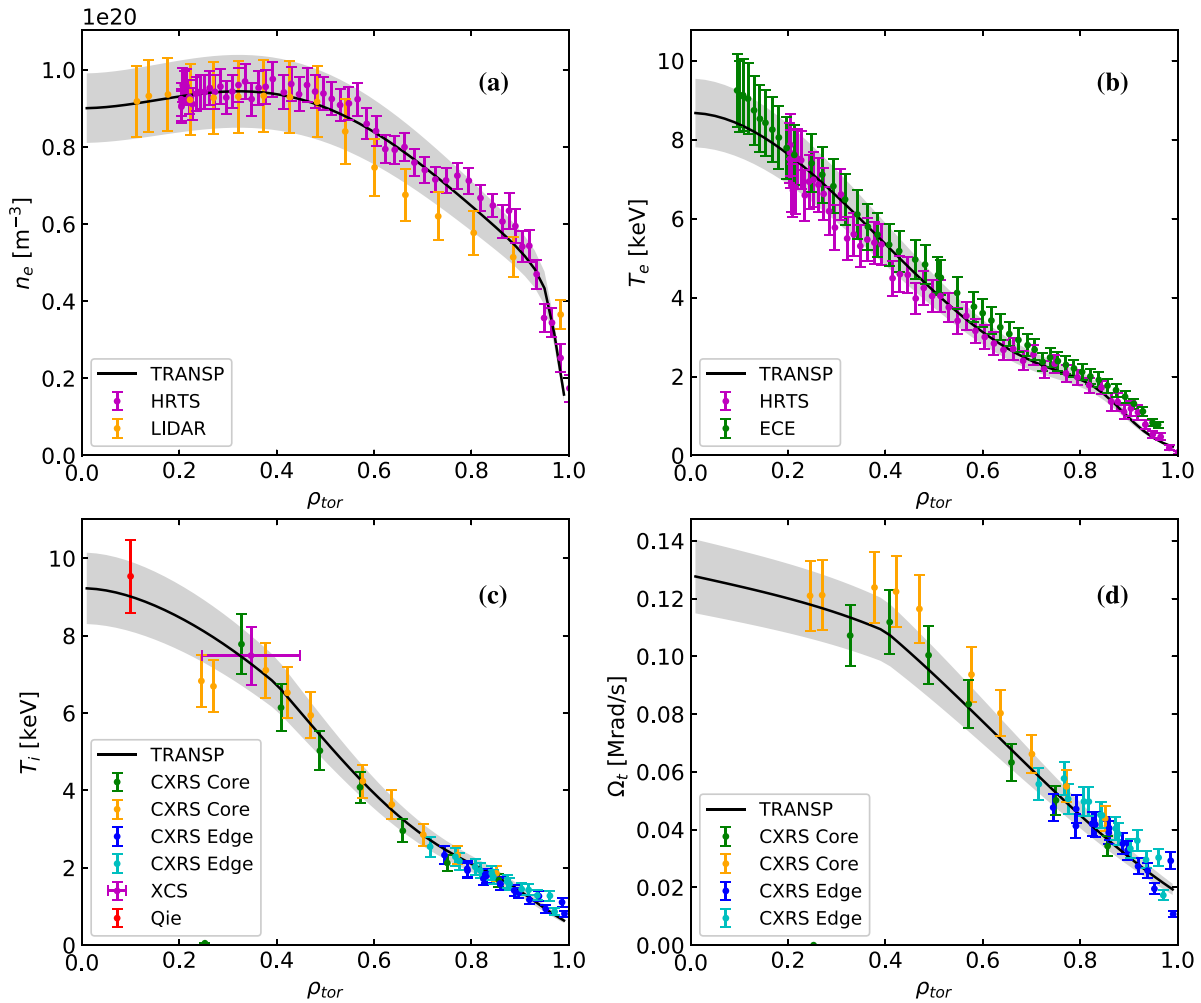


Figure 1. Example of a comparison between measurements (circles) and fits (solid black with 10% uncertainty) used as input in TRANSP interpretive simulations for the H-mode baseline scenario discharge #99863 at 9.55 s. Panels—(a): electron density with HRTS and LIDAR measurements, (b): electron temperature with HRTS and ECE measurements, (c): ion temperature with CXRS (core and edge) and high-resolution crystal x-ray spectrometer measurements (XCS, magenta), and ion-electron equipartition surrogate calculation (Q_{ie} , red), (d): toroidal rotation with CXRS (core and edge) measurements. The TRANSP's native ρ_{tor} radial coordinate, i.e. root of the normalized toroidal magnetic flux $\sqrt{\Psi_m}$, is on the x -axis. The grey shaded areas denote a 10% profile fit uncertainty (estimate).

measurements it is possible to obtain a good estimate of the impurity composition at JET [59], however such analyses are demanding and were not yet available for the majority of the database discharges. In order to unify the prescribed impurity composition across the database, we assumed a generic metallic wall mixture. That is a fixed value of 1% Be, stemming from CX analyses of representative discharges, and 0.02%–0.05% Ni, estimated by the high-resolution crystal x-ray spectrometer, with the remainder ascribed to W or Ne (depending on whether Ne puffing/seeding was employed in the discharge) based on a quasi-neutrality calculation constrained by visible Bremsstrahlung Z_{eff} measurements, assuming a flat profile. The following impurity composition assumption are made: high-Z (predominantly W) and mid-Z impurities (Ni representative of various metallic impurities in JET, originating from RF antennae coating) are assumed to mainly contribute to core radiation, with their core transport governed by neo-classical convection (JET high-performance hybrid discharge conditions with strong rotation and T_i decoupled from T_e) [60,

61]. On the other hand the low-Z impurities (e.g. Be, Ne, C) are assumed to be largely responsible for Z_{eff} , and with it core dilution, and can be approximated with a flat concentration profile with respect to n_e , due to the low sensitivity to plasma rotations. There was no additional anomalous particle transport imposed on the fast ion population, and no sawtooth model was applied. The interpretive simulations were performed with time-resolved kinetic profiles and external heating, while the presented database results are averaged over a one second interval in the steady highest-performing part of the discharges. The total energy confinement times generally vary between 250 ms and 350 ms for the DTE2 discharge database, which means that the presented parameters are averaged over a time interval that is a multiple of ~ 3 – 4 of τ_e .

2.3. Consistency checks

The quality of TRANSP results is largely dependent on the effort invested into rigorously preparing the input magnetic

equilibria and profiles, and ensuring basic output plasma parameters match the standard consistency measurements. The three basic global parameter consistency checks that are performed after every TRANSP analysis to ensure the quality of a given run are the line-integrated electron density, diamagnetic energy and neutron rates. It is worth noting that these three parameters represent the minimum required set, while more checks potentially need to be made, depending on the scenario type and physics aim. The TRANSP output contains a synthetic line-integrated electron density interferometer signal, which models the response seen by JET's eight laser interferometer channels [62]. A direct comparison to the measured interferometer data enables a quality check of the HRTS scaling, fitting, magnetic equilibrium mapping, and internal TRANSP interpolation procedures. Generally the interferometer line-of-sight measuring the electron density closest to the plasma core is used. The diamagnetic energy is calculated as part of the equilibrium reconstruction with EFIT++. W_{dia} is not output by TRANSP by default and is derived from the computed thermal W_{th} and fast ion perpendicular $W_{f\perp}$ energy components as $W_{\text{dia}} = W_{\text{th}} + 1.5 W_{f\perp}$ [63].

In D-T plasmas the total neutron yield Y_n is directly proportional to the fusion energy produced, i.e. $E_{D-T} = Y_n(\langle E_n \rangle + \langle E_\alpha \rangle)$, where $\langle E_n \rangle$ and $\langle E_\alpha \rangle$ are the average energies of D-T fusion neutrons at ~ 14.1 MeV and alphas at ~ 3.5 MeV. At JET the neutron yield is measured by absolutely calibrated fission chambers [4, 5]. The total yield is obtained as the time integral of the measured neutron rate R_n , which is defined as:

$$R_n = \int_V \frac{1}{1 + \delta_{ab}} n_a n_b \langle \sigma v \rangle dV, \quad (1)$$

i.e. a volume integral of the number of fusion reactions per unit time and unit volume, between two ion species with densities n_a and n_b , where δ_{ab} is the Kronecker delta, included to avoid the double counting of reactions when two ions of the same species are considered. The fusion reactivity $\langle \sigma v \rangle$ is defined as the integral over the ion velocity distribution functions f_a and f_b and the cross section for the reaction σ_{ab} :

$$\langle \sigma v \rangle = \int_{\mathbf{v}_a} \int_{\mathbf{v}_b} f_a(\mathbf{v}_a) f_b(\mathbf{v}_b) \mathbf{v}_{\text{rel}} \sigma_{ab}(\mathbf{v}_{\text{rel}}) d\mathbf{v}_a d\mathbf{v}_b, \quad (2)$$

where \mathbf{v}_a and \mathbf{v}_b are the velocity vectors of the interacting ions and \mathbf{v}_{rel} their relative velocity. Fusion reactivity can be computed by either semi-analytical or numerical integration techniques [64–66]. The total neutron emission in D-T plasmas with a mixed fuel and beam ion composition comprises neutrons originating from various combinations of fusion interaction between different isotopes and ion populations—most commonly these are divided into thermal ion interactions (*TH*), fast-thermal ion interactions (commonly labelled beam-target, *BT*), and fast-fast ion interactions (commonly labelled beam-beam, *BB*). The total neutron rate from equation (1) can be expanded into:

$$\begin{aligned} R_n(DT) = \int_V & \left(n_d n_t \langle \sigma v \rangle_{\text{TH}}(DT) + n_{\text{db}} n_t \langle \sigma v \rangle_{\text{BT}}(D \rightarrow T) \right. \\ & + n_d n_{\text{tb}} \langle \sigma v \rangle_{\text{BT}}(T \rightarrow D) + n_{\text{db}} n_{\text{tb}} \langle \sigma v \rangle_{\text{BB}}(DT) \\ & + \left[\frac{1}{2} n_d n_d \langle \sigma v \rangle_{\text{TH}}(DD) + n_d n_{\text{db}} \langle \sigma v \rangle_{\text{BT}}(D \rightarrow D) \right. \\ & + \left. \frac{1}{2} n_{\text{db}} n_{\text{db}} \langle \sigma v \rangle_{\text{BB}}(DD) \right] \Gamma_n + n_t n_t \langle \sigma v \rangle_{\text{TH}}(TT) \\ & + 2 n_t n_{\text{tb}} \langle \sigma v \rangle_{\text{BT}}(T \rightarrow T) \\ & \left. + n_{\text{tb}} n_{\text{tb}} \langle \sigma v \rangle_{\text{BB}}(TT) \right) dV, \quad (3) \end{aligned}$$

comprising D-T, D-D and T-T neutron contributions. The thermal fuel ion densities are denoted n_d and n_t , while n_{db} and n_{tb} are used for the beam population densities. The isotope's neutron rate contributions are additionally weighted by the number of neutrons produced in individual fusion interactions, namely D-T emitting one neutron per reaction, D-D $\sim 1/2$ neutron due to the $(n+{}^3\text{He})$ versus $(p+t)$ branching ratio Γ_n , and T-T two neutrons per reaction. The contribution of secondary neutron producing fusion reactions, such as D- ${}^3\text{He}$ and T- ${}^3\text{He}$, was not included in equation (3) due to their negligible yield. TRANSP calculates the total rate of neutron emission as well as its source components—thermal, beam-target and beam-beam fusion. In the paper we compare the calculated values against the total neutron rate measured by fission chambers. In addition to the three standard consistency checks, we also confirm that the measurements of the edge D-T fuel mix concentrations are preserved when prescribing the initial plasma composition in TRANSP. Therefore the divertor residual gas measurements of $n_d/(n_d + n_t)$ are compared to the TRANSP ion density output at the edge.

Figure 2 shows the measurements vs. calculation consistency plots for the global parameters of the DTE2 discharge database, in which we adopt a symbol notation corresponding to the scenario description at the beginning of section 2. The black dashed lines denote equality between the measurements and calculations, while the green dashed lines denote the combined experimental and computational uncertainty, evaluated to be around $\pm 10\%$ for n_e , W_{dia} , and $n_d/(n_d + n_t)$, and $\pm 25\%$ for the neutron yield. Both the line-integrated density and diamagnetic energy calculations in panels (a) and (b) align well with the measurements within the uncertainty, while showing signs of grouping according to the characteristics of the individual scenario. It can be seen that the baseline scenario experiments were performed at some of the highest densities achieved in D-T, in combination with the highest diamagnetic energy of ~ 10 MJ. Both the hybrid and T-rich scenarios were performed at mid-range density with diamagnetic energy clustered at around 8 MJ. The neutron yield comparison in panel (c) shows a more heterogeneous picture. One can observe that the bulk of the high performance pulse calculations, with neutron rates between 1×10^{18} and $4 \times 10^{18} \text{ s}^{-1}$, agrees with the measurements well. These mostly include

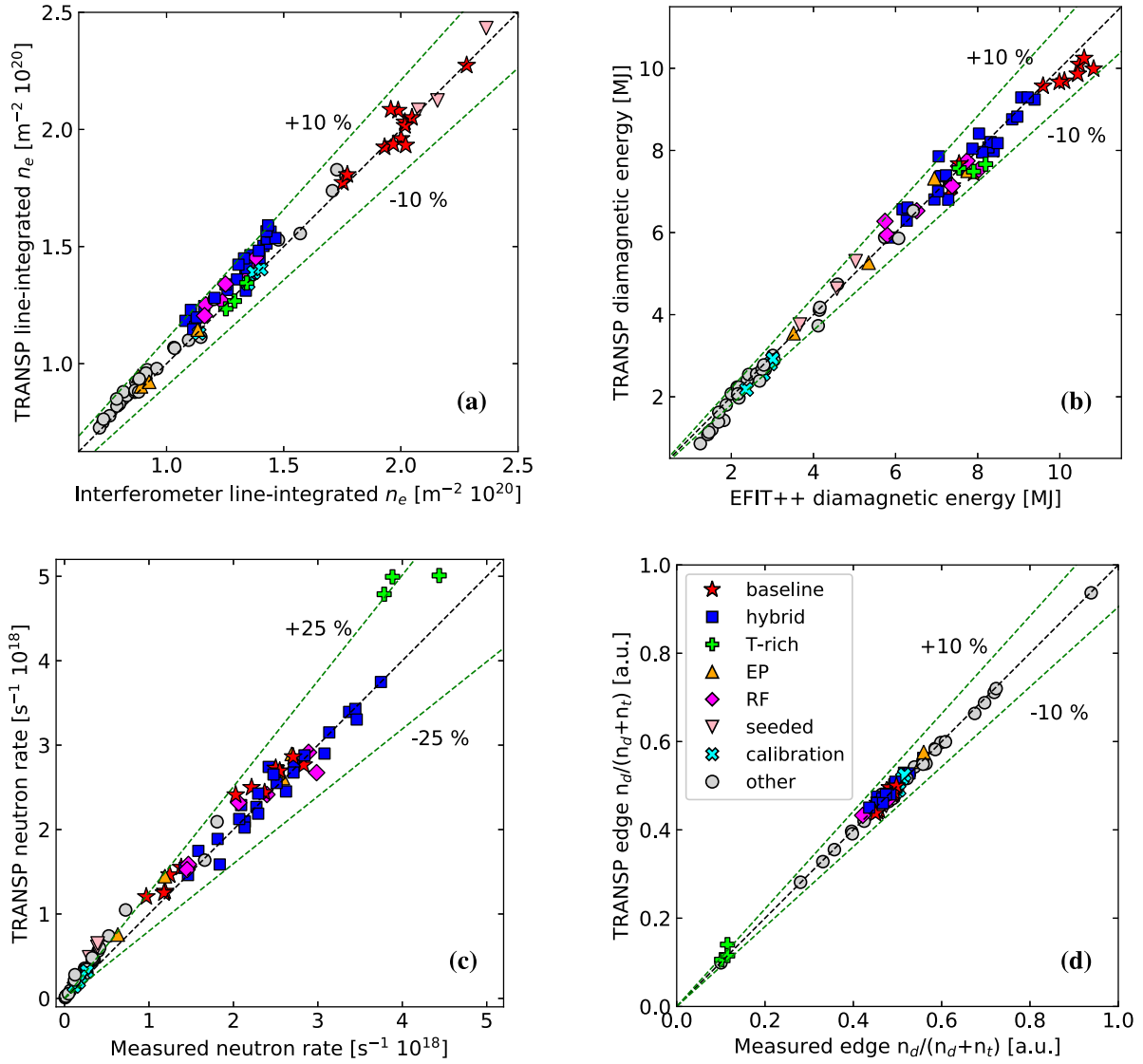


Figure 2. Consistency checks between measurements (x -axis) and TRANSP interpretive calculations (y -axis, 1 s average) for the DTE2 database—(a): core line-integrated electron density interferometer measurements and TRANSP synthetic diagnostic, (b): plasma diamagnetic energy W_{dia} computed by EFIT++ and TRANSP, (c): neutron rate fission chamber measurements and TRANSP calculations, (d): divertor residual gas measurements of the edge $n_d/(n_d + n_t)$ fuel mix and equivalent TRANSP calculations. The green dotted lines denote the combined experimental and computational uncertainty band. The graphs share the scenario type legend notation.

plasma scenarios in which the fusion power output was optimized throughout the campaign, e.g. baseline, hybrid, RF, and EP. On the other hand the lower power discharges with neutron rates below $1 \times 10^{18} \text{ s}^{-1}$ overestimate the measurements, as do the best performing, record T-rich pulses of DTE2. These produced neutrons at rates just above $4 \times 10^{18} \text{ s}^{-1}$, with calculations up to 25% higher than the measurements, but still within the estimated uncertainty. The additional edge fuel mix check presented in panel (d) shows that the prescribed edge fuel ion densities, after a dilution correction and TRANSP particle balance calculation, match the residual gas measurement. To summarize—a general observation for the four consistency checks is that a relatively good and satisfactory match between the measured and computed values is achieved, within the

estimated uncertainty, which forms a reliable basis for the conclusions we draw in the following sections.

3. Fusion performance analysis

In this section we present results obtained through a comparative analysis of the DTE2 discharge database. We focus on three major topics: (i) understanding the fusion performance drivers of various scenario types and trends of fusion power output optimization, and the overall performance of the interpretive fusion power calculations against absolutely calibrated measurements; (ii) assessing the fusion power computational uncertainty and its dependence on scenario type; (iii) overview

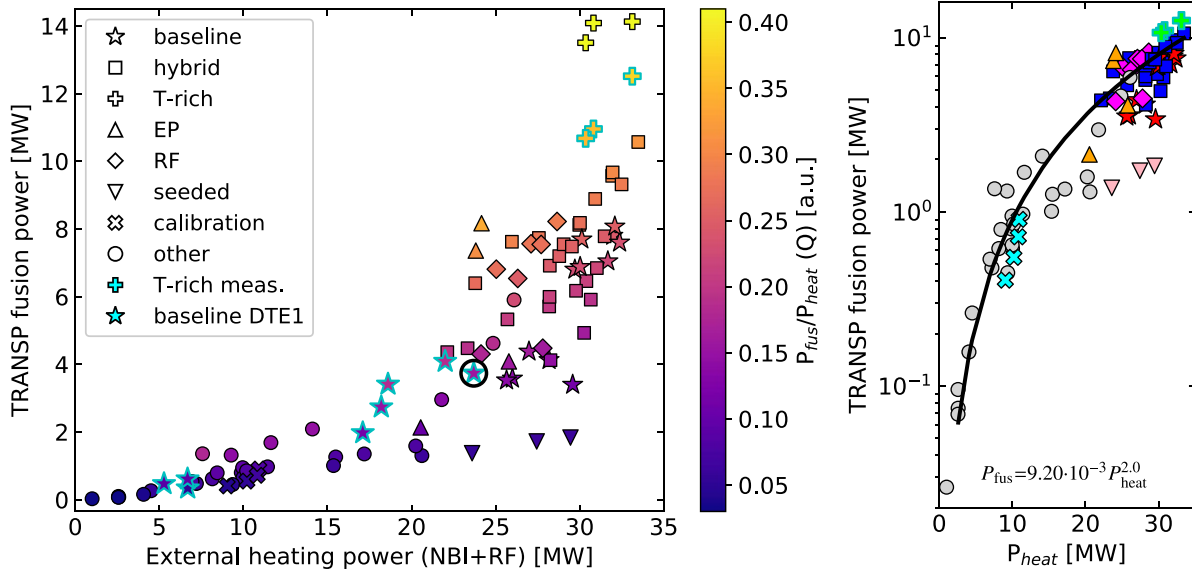


Figure 3. *Left:* TRANSP computed total fusion power versus the launched external NBI and RF heating power for the DTE2 database. The z -axis (colourbar) denotes the calculated fusion gain factor Q_{DT} , defined as ratio between the achieved fusion and external heating power. Fusion power and Q_{DT} using measurements are shown for the T-rich pulses (cyan edge pluses), in addition to TRANSP calculations for a subset of DTE1 baseline discharges are shown (cyan edge stars). The results are averaged over 3–4 τ_e . *Right:* TRANSP computed P_{fus} versus the launched P_{heat} , with their dependence fitted with a power-law function (solid curve, power in [MW]). The graphs share the scenario type legend notation.

of fusion alpha performance in the D-T experiments and the potential trends for future experiments.

3.1. D-T performance drivers

One of the goals of JET's DTE2 campaign with Be/W wall was to maximise the fusion power output compared to the preceding DTE1 achievements in a sustained way [19, 22, 23]. Based on results from deuterium campaigns with the ITER-like-wall, two steady plasma scenarios with the potential of delivering the objective were identified—the baseline and hybrid H-mode discharges. Modelling work was done to assess the level of expected fusion power output based on the best performing deuterium discharges. This was done with two methods—interpretive D-T equivalent fusion power calculations, in which the plasma kinetic profiles were assumed to be the same as in D with the fuel mix altered to 50-50 D-T, and through predictive modelling. The latter was based on coupling of core integrated modelling (TRANSP, JINTRAC, ETS) and quasilinear turbulent transport codes (TGLF, QuaLiKiz), in which the kinetic profiles are evolved taking into account phenomena like the isotope effect, through energy exchange or $E \times B$ shear stabilization, and fusion alpha heating [10, 20, 67, 68]. Both methods agreed in predicting the extrapolated fusion output to reach levels between 9 ~ 15 MW with uncertainties of up to ± 2 MW, at a nominal total external heating power of 40 MW. It was observed that the predictive extrapolations of the fusion power displayed a strong power function relationship with the external plasma heating.

The high fusion performance branch of DTE2 experiments has confirmed these observations, albeit with the combined NBI and RF power reaching maximum values of around

35 MW [25, 28, 30]. In figure 3 we display how the one-second-averaged TRANSP computed power depends on the total external heating power P_{heat} , launched by the heating systems, for the DTE2 modelling database. A clear power-law dependence can be seen between the two quantities, with the fusion power gain rate increasing with added heating power. The computed exponent of the fitted function for the entirety of the DTE2 database following a P_{heat}^λ dependence, shown in the right-hand side graph of figure 3, is $\lambda = 2.0 \pm 0.3$ (for heating power in MW). Although the fitted function matches the P_{fus} trend relatively well for the majority of the database, considering the fusion power spans over more than two orders of magnitude, one can observe that individual scenarios show signs of branching and display varying fusion rise rates. The baseline scenario's best-performing discharges are clustered at around 8 MW of fusion power, and are located on the lower part of the power curve, meaning that more heating power is required to match the output of other high-performance scenarios. One can observe that the hybrid power branch average is approximately 20% higher compared to the baseline for the same input power, reaching a maximum fusion power output of ~ 10 MW. The highest-performing discharges of the campaign were the hybrid-like T-rich plasmas, in which the fuel mixture and beam settings were optimized to maximize fusion reactivity. This was achieved by developing a scenario with the beam species in deuterium-only, and the thermal ion species being tritium, in order to exploit the favourable fast deuterium \rightarrow thermal T reactivity at beam injection energy of ~ 110 keV, typical for JET's NBI system [30, 69]. This scenario yielded the largest fusion energy output ever at 59 MJ, with high P_{fus} sustained for 5 s. Two of the modelled EP scenario discharges, employing a hybrid-like scheme using only

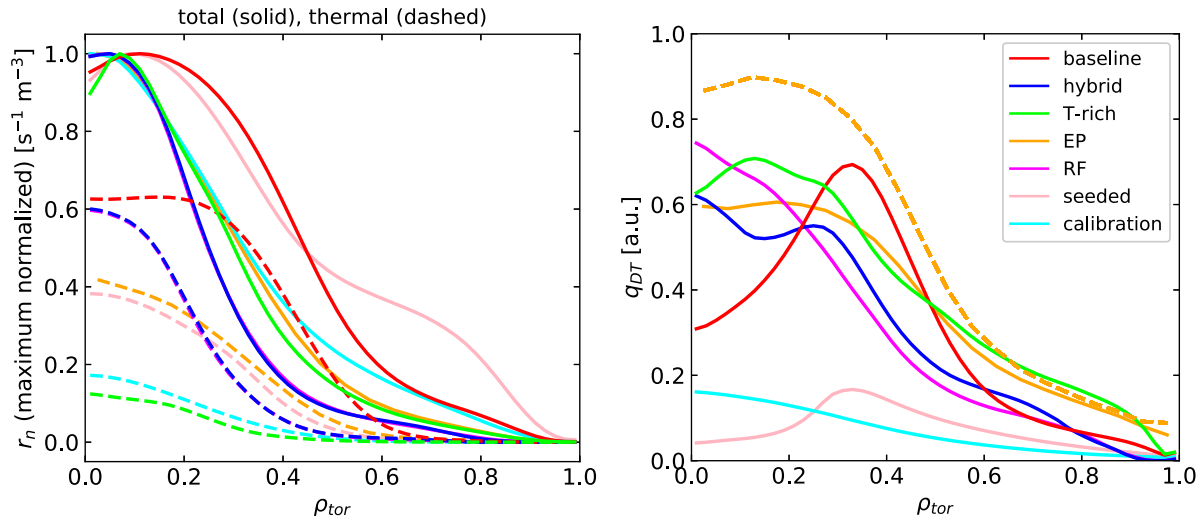


Figure 4. *Left:* TRANSP computed total (solid) and thermal (dashed) neutron rate density profiles r_n , normalized to the total maximum value. *Right:* computed local fusion gain factor q_{DT} , both plotted on the ρ_{tor} radial coordinate. In both graphs one-second-averaged results for selected best performing discharges of individual DTE2 scenarios are shown (solid—baseline #99948, hybrid #99912, T-rich #99965, EP #99802, RF #99884, seeded #99621, neutron calibration #99812), in addition to the highest computed transient q_{DT} (dashed—EP #99802). The results are averaged over 3–4 energy confinement times τ_e . The graphs share the scenario type legend notation.

NBI heating with afterglow, produced the highest transient fusion power output and central T_i per MW of external heating in DTE2 [32]. In figure 3 the two EP-hybrid discharges are located in the upper part of the discharge cluster, indicating a high fusion power rise rate. The D-T Ne-seeded experiments were not optimized for high fusion power production, but rather demonstrated the compatibility of the scenario with D-T and a Be/W wall. Therefore these discharges exhibited some of the lowest fusion performance per P_{heat} , which was a result of high pedestal and core n_e and radiated power—a combination of these conditions spelled a low beam penetration and core ion temperature. The z -axis represents the fusion gain factor Q_{DT} defined as P_{fus}/P_{heat} (input/launched power averaged over a multiple of 3–4 of τ_e), which is seen to steadily rise with increasing performance. The calculated maximum one-second-average Q_{DT} for the baseline, hybrid and T-rich scenarios are 0.26, 0.32 and 0.41, respectively. Figure 2 shows that the calculated fusion yield of the T-rich discharges is over-predicted, contrary to other high-power DTE2 discharges, discussed in detail in sections 3.2 and 4. In order to represent the rising trend of the fusion gain better, the fusion power and Q_{DT} for the T-rich pulses are plotted using the measurements as well, denoted with cyan edge pluses. One can observe that this results in a better agreement with the computed fusion power trend, with a maximum achieved Q_{DT} of around 0.35. One of the highest transient Q_{DT} values of ~ 0.45 was achieved by the EP-hybrid scenario. For comparison we plot a selection of TRANSP calculations for steady baseline discharges from the JET-C DTE1 campaign (cyan edge stars) [14], with the P_{fus} and Q_{DT} rise trends similar to the bulk of the DTE2 cluster. If the DTE1 performance is extrapolated to higher P_{heat} , we see that the trend matches the baseline scenario JET-ILW results, but appears to be slightly higher, potentially due to differences in confinement observed between the two wall configurations [70–72]. The best performing DTE1 steady baseline discharge

#42982 achieved a fusion power output of ~ 4.6 MW and $Q_{DT} = 0.19$ (encircled).

On the left-hand side of figure 4 the computed total and thermal neutron rate density profiles r_n are shown, normalized to the total maximum value. Representative discharges of individual DTE2 scenarios with some of the highest fusion power are plotted (baseline #99948, hybrid #99912, T-rich #99965, EP #99802, RF #99884, seeded #99621, calibration #99812). Based on the shape of the emissivity profiles, the discharges are roughly divided into two groups: (i) discharges with broader emissivity profiles, which are the higher (core and pedestal) density baseline and Ne-seeded scenarios. Due to the higher n_e the beam penetration and beam density peakedness are low. In the case of the Ne-seeded discharge, which is highly beam-target dominated, the broadness is highest with a clear beam-deposition-driven local peak at the edge. In the baseline discharges this effect is less pronounced because the core ion temperature is significantly higher, contributing to a dominating thermal fusion drive and increasing peakedness. (ii) Discharges with a peaked neutron emissivity profiles, which is a consequence of low n_e , higher beam penetration and peaked ion temperature profiles, with a generally lower thermal-ion fusion contribution. The majority of these discharges exhibit a dominating beam-target fusion component.

In the right-hand side graph of figure 4 the computed radial profiles of the local fusion gain factor q_{DT} are shown. It is computed as the ratio between the profiles of fusion power (proportional to r_n) and plasma heating densities p_{fus}/p_{heat} . The radial distribution of fusion reaction rate for the majority of discharges is largely peaked in the core within $\rho \lesssim 0.4$. But because this area is volumetrically much smaller than the edge, the local fusion gain factor can significantly differ from the integrated global Q_{DT} value. Thus one can see that all the highest performing scenarios achieve a peak q_{DT} between

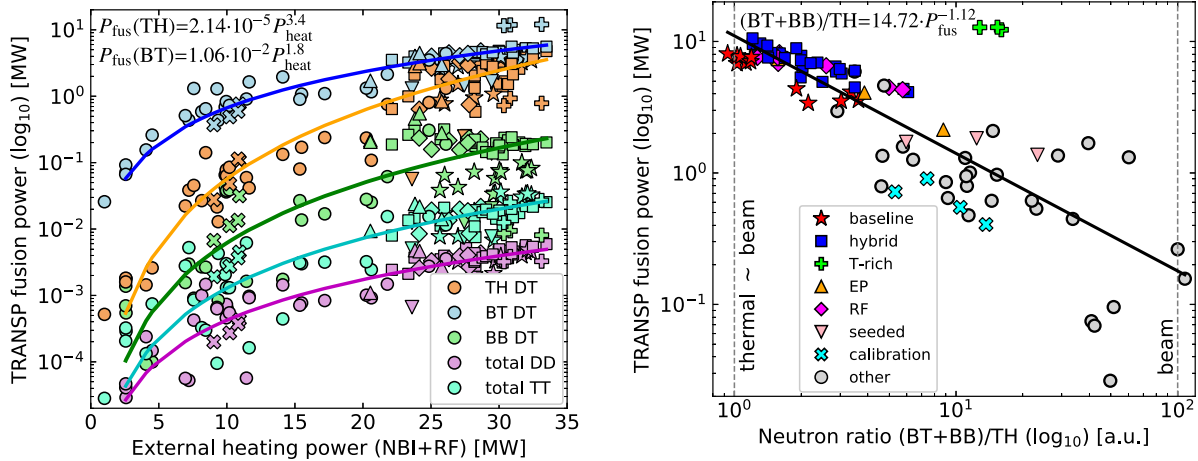


Figure 5. *Left:* computed fusion power components—thermal D-T (orange), beam-target D-T (blue), beam-beam D-T (green), total D-D (magenta) and total T-T (cyan)—versus the launched external NBI and RF heating power for the DTE2 database. The power increase rates for individual components are fitted with a power-law function (solid curves, power in [MW]). *Right:* computed total fusion power versus the ratio between the neutrons emitted from beam-induced fusion and thermal fusion neutrons. Discharges with beam-dominated fusion performance are located on the right-hand side of the graph, while the discharges on the left have equal thermal and beam contributions. The distribution is fitted with a power-law function (solid black curve, power in [MW]). The graphs share the scenario type legend notation.

0.6 ~ 0.75 in the core region, while the low power discharges peak at q_{DT} just below 0.2. A clear difference can be seen in the profiles depending on the electron density—both the baseline and Ne-seeded discharges with high n_e exhibit hollow q_{DT} profiles with peaking at $\rho \sim 0.35$, which is a consequence of broad neutron emissivity profiles and low beam penetration with hollow deposition profiles. In contrast to the one-second-averaged q_{DT} profiles, the highest transient fusion gain, averaged over 20 ms (dashed line, integration time $\ll \tau_e$), is computed for the EP-hybrid discharge #99802 with a peak value of $q_{DT} = 0.9$ at $\rho \sim 0.1$. The results agree with the analysis of DTE1 experiments, specifically the record sustained baseline #42982 with a maximum q_{DT} of 0.7, but did not repeat the transient $q_{DT} \gtrsim 1.2$ observed in the hot-ion H-mode discharges that locally exceeded the break-even condition [73].

TRANSP offers insight into the neutron emission characteristics of the modelled discharges, enabling an understanding of the different scenarios' underlying fusion performance drivers. In the left-hand side panel in figure 5 we display the contributions of the various fusion reaction components to the total fusion power (expanded on in equation (3)), dependent on the total external heating power P_{heat} . We can generally observe that individual fusion components follow a clear power-law trend, which is confirmed by fitted functions (solid lines). It is beam-target fusion (blue) that largely drives JET's D-T performance over the range of heating power. The thermal component (orange) becomes increasingly more prominent at higher heating power, i.e. at ~ 10 MW the BT components is still an order of magnitude larger than TH in average, while the ratio of BT/TH fusion power decreases to a value between 3 and 1 at heating power above 30 MW. The computed exponents of the fitted functions, following a P_{heat}^λ dependence, are $\lambda(TH) = 3.4 \pm 0.6$ and $\lambda(BT) = 1.8 \pm 0.4$ (for heating power in MW). The beam-beam component (green) remains relatively low in most of the D-T discharges, which is due to the

rollover of the D-T cross-section for energetic fuel ions—unlike in deuterium plasmas, there are no D-T fusion performance benefits to evolving an extremely energetic fast ion population. The BB component values display a relatively large spread with respect to the fit due to a strong variation in beam density between the different scenarios, and plateau at a fusion power of around 200 kW for higher heating power, where they are an order of magnitude or more smaller than both BT and TH, in average contributing to $\lesssim 5\%$ to the total fusion power. Similarly the calculated D-D (total reactant energy of 3.65 MeV) and T-T (total reactant energy of 11.3 MeV) fusion power components are low in all discharges due to the low cross-sections compared to D-T, with their combined neutron yield contribution below 1%.

An important milestone on the path to achieving burning plasma conditions in tokamaks is the development of plasma scenarios in which the majority of fusion interactions is triggered by thermal ions. This would mean that the fuel fast ion concentration in the plasma is low and does not play a significant role either in heating or directly triggering fusion. The heating would ideally be bootstrapped by fusion alpha particles, enabling a high enough electron and ion temperature to sustain the burning reaction. The ratio between beam-induced and thermal D-T neutron yields gives one of the key insights into how JET's various DTE2 scenarios are performing with respect to achieving such conditions, and displays to what degree the fusion performance is dependent on the presence of external plasma heating. This is especially relevant for JET, which was not designed to achieve large fraction of alpha heating. We display a graph of the relation between the computed total fusion power and the (BT+BB)/TH yield ratio for the DTE2 database in the right-hand side panel of figure 5. The ratio reaches a maximum at around 100 on the right-hand side of the x-axis where discharges with dominating beam-driven fusion are located. On the left-hand side of

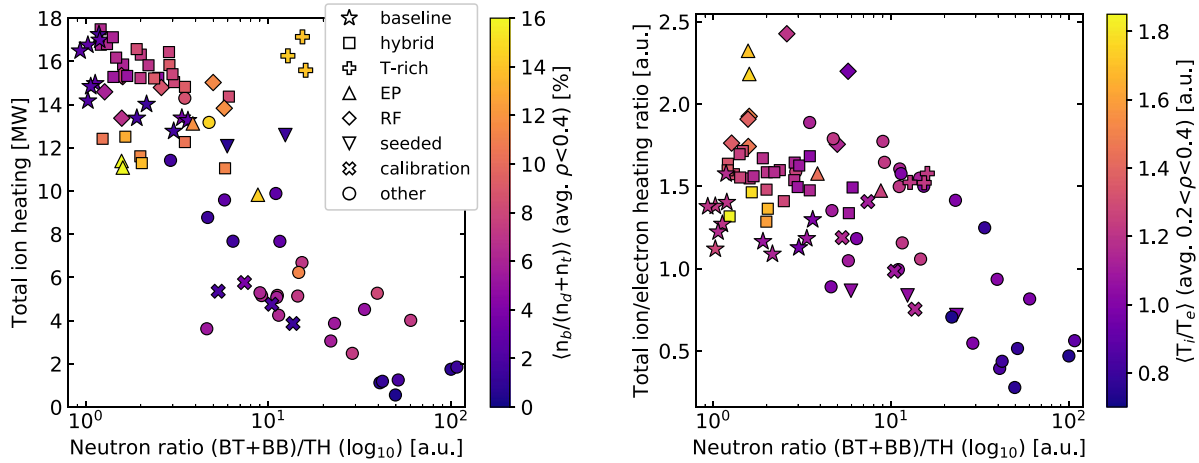


Figure 6. *Left:* computed total ion heating versus the ratio between the neutrons emitted from beam-induced and thermal fusion for the DTE2 database. The z -axis (colourbar) denotes the ratio between the beam and D-T fuel ion density in the plasma core (averaged over $\rho < 0.4$). *Right:* computed ratio between the total ion and electron heating in dependence of the ratio between the neutrons emitted from beam-induced and thermal fusion. The z -axis (colourbar) denotes the ratio between the ion and electron temperature in the plasma core (averaged over $0.2 < \rho < 0.4$). The graphs share the scenario type legend notation.

the graph discharges with equal thermal and beam-induced fusion are clustered. Interestingly one can observe that the distribution of the discharges in the graph indicates that the $(BT+BB)/TH$ ratio is inversely proportional to the external heating power, with the high performing discharges exhibiting larger thermal contributions compared to the low P_{heat} discharges. The baseline discharges have achieved the highest consistent $(BT+BB)/TH$ yield ratio of ~ 1 , seen clustered on the top left of the graph. The hybrid discharges exhibit a spread of the yield ratios with the average between $0.8 \sim 0.9$. The database trend was fitted with a power-law function—extracting the dependence of the neutron yield ratio to P_{fus}^λ , we obtain an exponent of $\lambda((BT+BB)/TH) = -1.12 \pm 0.09$ (for fusion power in MW). Assuming the external heating power would reach its nominal installed maximum at 40 MW, the baseline discharges would be expected to reach between 13 and 14 MW of fusion power and an extrapolated $(BT+BB)/TH$ yield ratio of around 0.55, which indicates an approach to a thermal fusion dominated regime. It can be observed that the T-rich discharges do not follow the trend set by the bulk of the high performance discharges, with their record fusion output being highly beam-driven. This is due to the fact the main scenario development branch focused on 50-50 D-T plasma and mixed D-T beam species, in contrast to the T-rich scenario that optimized non-thermal D-T fusion.

In order to explain the observed discharge distribution with respect to the $(BT+BB)/TH$ yield ratio, we analyse the TRANSP computed electron and ion power balance. In the left panel of figure 6 we plot the relationship between total ion heating and the yield ratio, with the ratio between core beam and fuel ion densities on the z -axis. We observe that the discharge distribution is similar compared to the right-hand side graph in figure 5, i.e. the low power pulses are in the bottom right, spanning towards the best performing pulses in the top left. This is in line with the observed thermal component increase, confirming that the ability to drive and

improve fusion performance in JET is linked to efficient bulk ion heating in ~ 50 -50 D-T plasmas. The fraction of power coupled to the ion channel from a positive-ion based NBI heating system improves with the increase of the external heating power. There are additional mechanisms favouring ion heating over its electron counterpart, such as increased beam critical energy and decreased collisionality, connected to increasing T_e with rising total heating power input. The beam critical energy is defined as $E_{\text{crit}} = 14.8 \cdot T_e [\text{keV}] A_b (\sum_i \frac{n_i Z_i^2}{n_e A_i})^{2/3}$, where A_b is the mass of injected beam neutrals, and A_i and Z_i the mass and charge of the plasma ions. The highest computed ion heating is observed for the high-power baseline, hybrid and T-rich scenarios at around 17 MW, which is approximately half of the total external heating power applied. The radiated power fraction of the database discharges varied between $0.2 \sim 0.35$. Although the T-rich scenario exhibited one of the highest total ion heating values, and achieved relatively high core T_i , its thermal fusion component remains low, as the scenario was explicitly optimized for non-thermal D-T fusion (the plasma is predominantly composed of thermal tritium, with low thermal deuterium concentration, resulting in the density product $n_d n_t$ being approximately a factor of 2 lower than that of a 50-50 D-T plasma). The core-averaged relative concentration of the beam population with respect to fuel ions $\langle n_b / (n_d + n_t) \rangle$ shows little correlation to the yield ratio or fusion performance and remains below 6% for the majority of the database. The highest computed core beam concentration was achieved in the T-rich and EP-hybrid scenarios at above 10% due to low n_e . At the lowest electron density and high core beam concentration the EP-hybrid discharges display a large total ion heating, resulting in some of the highest on-axis T_i measured in the DTE2 campaign of $\gtrsim 16$ keV. The time-averaged $(BT+BB)/TH$ ratio of these discharges is around 1.6, while EP discharge #99801 transiently achieved one of the largest relative TH contributions, with $(BT+BB)/TH = 0.8$.

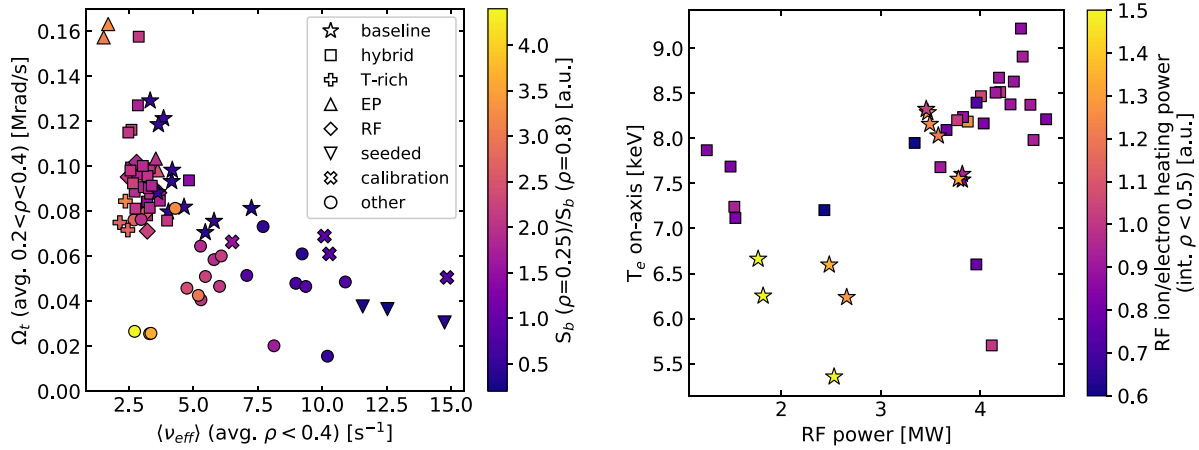


Figure 7. *Left:* fitted core-averaged toroidal rotation frequency versus the effective collisionality for the DTE2 database. The z -axis (colourbar) denotes the ratio between the total beam particle source in the core ($\rho = 0.25$) and at the edge ($\rho = 0.8$). *Right:* on-axis electron temperature fits versus the launched RF power for baseline and hybrid DTE2 discharges only employing H minority RF heating. The z -axis (colourbar) denotes the ratio between the ion and electron RF heating power integrated within $\rho < 0.5$. The graphs share the scenario type legend notation.

In the graph on the right-hand side of figure 6 we look at the decoupling between the electron and ion heating channels. Specifically, we plot the relation between the ratio of total ion over electron heating and the (BT+BB)/TH yield ratio, with the average ratio between core T_i and T_e on the z -axis. It can be seen that there is a clear difference between the low- and high-performing discharges, with the ion to electron heating ratio rising steadily above unity with increasing fusion output and thermal fusion contribution, reaching maximum values above 2. The average ion over electron core temperature ratio is weakly correlated to the heating ratio—we can observe that the lower power discharges exhibit $T_i/T_e \leq 1$, while the core ion temperature starts showing signs of decoupling for higher performing pulses, e.g. the ratio varies between 1.1 \sim 1.3 for the baseline and hybrid discharges. One can observe an increase in core T_i/T_e even within individual scenarios with rising external heating power (moving towards the left-hand side of the graph). We can explain the observations with the following reasoning: with increasing external heating, both the electron and ion temperature rise, but it is T_e that plays the role of the driver due to its linear connection to the beam critical energy, which determines the threshold for the favourable flow of beam energy to the ion channel, and the proportionality of the beam-slowning down time and density to $T_e^{1.5}$. With increasing beam power the fraction of beam power to the ions increases as well, which in addition to the larger critical energy bootstraps the core ion heating. The temperature decoupling is kept in check by the power balance equipartition term q_{ie} . Additional favourable mechanisms for the decoupling between the temperatures were recognised, such as the increase in plasma rotation due to increased beam torque and low gas puffing, and its effects on ITG stabilization [74]. We note that the various RF scenarios, extensively tested during DTE2 [35], also display a relatively high ion/electron heating ratio and T_i/T_e consistently above unity. This can be partially ascribed to the positive effects of various RF heating schemes—in addition to direct heating of the electron population, an RF fast ion population is

formed, initially transferring energy to electrons through collisions. The efficient electron heating raises T_e and the critical energy, and decreases the collisionality, which leads to a formation of a more energetic fast ion tail. A combination of these effects efficiently bootstraps ion heating, both by the beams as well as the formed energetic RF tail. The two modelled EP-hybrid discharges display a remarkable core T_i/T_e ratio of ~ 1.6 , enabled by larger beam penetration due to low electron density and collisionality, and high core rotation. The operational regime relevant for ITER and study fusion pilot plants, exploring burning plasma conditions, is designed to be electron heating dominated with a (BT+BB)/TH yield ratio $\ll 1$. The two conditions have not been simultaneously observed in JET DTE2 discharges, due to the fact that direct electron heating systems such as ECRH are not employed, while NBI provides dominant ion heating at high heating power. Thus the discharges follow a trend of rising ion heating in favour of the electron channel with increasing external heating power, reaching an average total ion/electron heating ratio of ~ 1.5 .

In the left-hand side graph of figure 7 we look at the relationship between the fitted toroidal rotation frequency averaged in the core ($0.2 < \rho < 0.4$), and the effective core collisionality that is proportional to $\langle n_e \rangle / \langle T_e^{1.5} \rangle$, volume averaged within $\rho < 0.5$. The collisionality of the majority of best performing pulses is relatively low, i.e. between the values of 2–5, which is in agreement with the conditions that are needed to drive a high T_i/T_e ratio. Such an example are the EP-hybrid discharges which, at relatively low density and high T_e , exhibit the lowest collisionality of the database, in addition to a combination of a large core rotation and core beam heating. A large portion of the lower power pulses display $\langle \nu_{\text{eff}} \rangle$ above 5, reaching maximum values of around 15. Core rotation inversely depends on plasma density and collisionality, which is demonstrated with the $\Omega_t(\langle \nu_{\text{eff}} \rangle)$ trend in the graph. At low collisionality the edge-core rotation coupling is weak, which can, in combination with the presence of large beam momentum transfer on-axis, result in high core rotation, such as seen in

some hybrid and EP discharges. In the baseline discharges the higher pedestal density results in increased beam angular momentum deposition at the edge, increasing the edge rotation frequency. A slightly higher collisionality in these discharges enables higher momentum transfer to the core, which in combination with particle fuelling effects helps to keep the rotation relatively high [74]. The rotation angular frequency thus has a dependence on the scenario type, with the highest fusion output discharges displaying values above $\sim 7 \times 10^5 \text{ rad s}^{-1}$. Seven database discharges do not have available rotation data due to lack of CX measurements, all of them at low heating power. A finite Ω_t also directly affects the beam-target fusion reactivity, due to the fact that the relative ion velocity term, introduced in equation (2), changes. Whether v_{rel} increases or decreases depends on the passing or counter-passing nature of the target ion. TRANSP and ASCOT simulations have shown that the effect of including rotation profiles on the neutron yield was up to 10% in deuterium high performance plasmas, with the addition of rotation generally resulting in a net yield decrease [75]. Further investigations into the effects of rotation in high performance D-T plasmas are presented in [30]. On the z -axis we display the ratio between the beam deposition source in the core (at $\rho = 0.25$) and at the edge (at $\rho = 0.8$), which is a measure of the beam deposition profile peakedness. There is no clear correlation with the collisionality, but there is an observable dependence on the electron density, resulting in differences between the high performance scenarios. The baseline and seeded discharges with the highest n_e in the campaign have the lowest beam peakedness with values below 1, meaning that the fast beam ion deposition profiles are hollow and peak at the edge. On the other hand the hybrid discharges display deposition ratio values of $\gtrsim 1.5$ at lower electron densities. The T-rich experiments have some of the most peaked profiles, owing not only to hybrid-like n_e , but also to the fact that the injected beams are pure deuterium, which has a larger penetration depth due to its lower mass—a single-isotope beam configuration was used for other pulses with the highest peakedness as well.

The graph on the right-hand side of figure 7 displays the volume averaged ($0 < \rho < 0.5$) core electron temperature versus the launched RF power, with the colour-coded symbols indicating the ratio between ion and electron RF heating power. The latter includes both direct RF wave absorption and collisional heating by minorities to both channels. The data shown in the graph is based on a reduced set of baseline and hybrid discharges only. The subset was chosen because the RF H minority scheme was consistently applied in these scenarios, using a relatively constant minority concentration of $X[H] \sim 2\% \pm 1\%$, at similar NBI heating power. In other scenarios, e.g. T-rich and RF, different minority species and concentrations were employed, rendering the discharges unsuitable for this comparison. The plot shows that the core electron temperature increases with RF power for the H minority scheme. In both baseline and hybrid discharges it can be seen that the central T_e increases by around 1 keV per \sim additional 2 MW of RF power applied. In absolute terms the average value of the lowest RF power injected is around 2 MW, while the maximum is approximately 4.5 MW. The baseline

discharges exhibit a consistently higher ratio of ion to electron heating, compared to the hybrid discharges. In the baseline scenario the ratio of ion over electron core heating consistently reaches values between $1.2 \sim 1.5$, while the hybrids display a lower spread with an average value of around 0.85. The hybrid discharges achieved core electron temperatures higher than those of the baseline shots in average at lower RF power, however the latter seem to exhibit a steeper T_e rise rate. An interesting observation is that at low P_{RF} and T_e the ion over electron heating is calculated to be higher than at high P_{RF} and T_e for baseline discharges, which is contrary to what is expected. Namely as the critical energy of fast H ions decreases with dropping T_e , one would anticipate that if the minority population is accelerated to the same energy more power would flow to the electrons. The hybrid discharges are found to display a relatively constant ion over electron heating ratio over the analysed RF power range. In addition to the fundamental H minority RF heating in the selected pulses, a part of the RF power is absorbed on fast D-beam ions as well, which are accelerated via the second harmonic Doppler broadened resonance. Acceleration of energetic D or T ions by RF waves, i.e. so-called synergistic effects, has been shown to improve D-T fusion performance to some extent [33, 76]. For instance, extremely efficient ion heating was demonstrated in dedicated T-rich experiments, with RF power densities on bulk and fast ions being a factor of 2–4 higher than those deposited on electrons. Other DTE2 RF heating schemes, relevant for ITER D-T RF operation, include fundamental resonance on D ions, ^3He minority and second harmonic T heating [35], as well as the 3-ion T-(^9Be)-D scheme. In the latter a resonant ion-ion hybrid layer is formed due to the presence of a minority ion species with an intermediate charge-to-mass ratio with respect to the majority D-T ions, in this case JET's intrinsic metal wall impurity ^9Be [77]. All of the above-mentioned schemes have certain advantages and disadvantages. For instance, the advantage of fundamental D heating and second harmonic T heating is that the RF waves directly heat the fusion reactants in a D-T plasma, impacting fusion performance. However the D-T reactivity for fast-thermal ion interactions peaks at around 130 keV for deuterons and 190 keV for tritons, after which it decays and reduces by approximately a factor of 2 at energies of 300 keV. This means that a fine balance needs to be struck between efficiently RF-accelerating ions, ensuring both bulk and fast ion heating, yet not producing a fast ion population that is too energetic, which could overshoot the maximum of D-T reactivity. In highest-performing deuterium plasmas the direct contribution of RF fast ions to fusion performance was found to be between $10\% \sim 15\%$, with the beam synergy effect having a large role due to a monotonously increasing D-D cross-section [15, 18, 45, 78]. In D-T plasmas the direct performance contribution of RF is found to be smaller, varying between $3\% \sim 5\%$ for synergy fast ions in baseline and hybrid discharges [76, 79, 80], to approximately 10% for fundamental D large minority heating in the T-rich experiment, discussed in more detail in section 4 and other dedicated studies [30].

Next an analysis of the time evolution of fusion performance for two representative high-power discharges is presented, the baseline #99863 and hybrid #99950. These

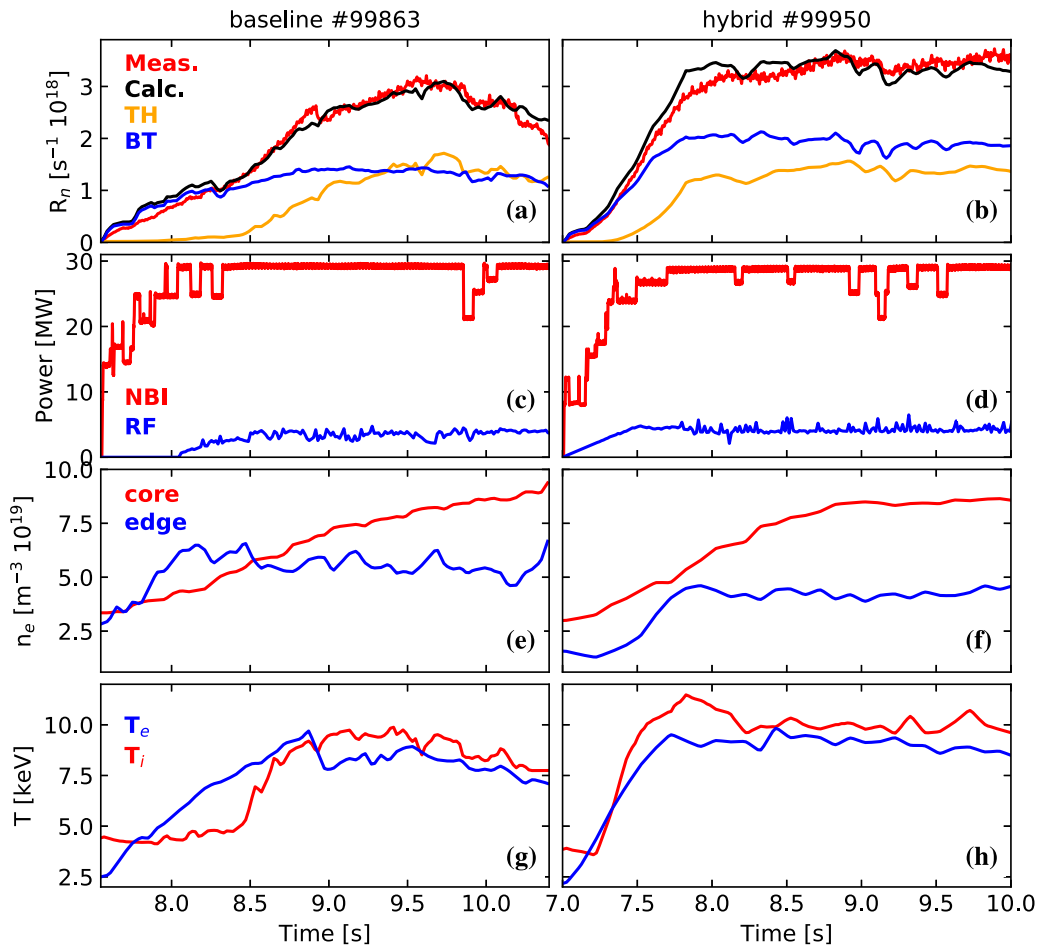


Figure 8. Comparison of plasma parameters for the baseline #99863 (*left*) and hybrid #99950 (*right*) D-T discharges [25, 28]. Panels (a) and (b) display a comparison between the time-evolved total neutron rate measurement (red) and the TRANSP calculation (black), which is further split into the thermal (orange) and beam-target (blue) components. Panels (c) and (d) show the NBI (red) and RF (blue) power waveforms, with the core (red, $\rho = 0.2$) and edge (blue, pedestal top at $\rho = 0.85$) electron density fits shown in panels (e) and (f). The on-axis electron (blue) and ion (red) temperature fits are shown in panels (g) and (h).

two discharges were chosen because both were performed at a fuel mixture close to 50-50 D-T, displayed similar T_e and T_i at the start of the heating phase, and employed NBI and RF heating with matching power, both using the H minority RF scheme. We focus on the differences in the evolution of their neutron yields, caused by discrepancies in plasma conditions, from the beginning on the heating phase to the point of reaching steady performance. Figure 8 displays a comparison of selected plasma parameters, from top to bottom neutron yield, external P_{heat} , local core and edge n_e , and on-axis T_e and T_i , with a shared y-axis between the horizontal graph panels.

Baseline scenario: the time interval [7.55, 10.4] s from the beginning of NBI heating to a point of performance deterioration preceding a disruption is shown. After the beam is turned on the BT fusion component starts to rise and remains dominant for one second. It is the n_e and T_e that govern the fusion performance conditions in this phase. One can see that there is a relatively large increase in edge n_e at the beginning, limiting the beam penetration depth and the rise rate of the BT component. The T_e is dependent solely on NBI power

at the beginning, with its rise rate relatively low. Due to the dominant inverse power-dependence of collisionality to T_e the beam energy distribution is slowly becoming more energetic, favourable for fusion, which in combination with an increasing core ion density drives the beam-induced yield increase. It is not until ~ 8.5 s that T_i also starts increasing, driving the TH yield component. This occurs due to a combination of factors—the RF heating is turned on at 8 s, which supports the power flow into the electron channel, bootstrapping T_i through an increase in critical energy. There is also a drive in bulk ion heating through fast H minority slowing-down. Collisionality is still not stabilized and is not low, therefore the RF tail is not expected to be highly energetic. There is an additional effect of RF power deposition on D-NBI ions through the Doppler-shifted second harmonic resonance, boosting BT fusion directly by energizing beam ions and contributing to bulk temperature increase. A large sawtooth event at 8.9 s strongly affects T_e and caps its on-axis value to ~ 8 keV. This also slows the rise rate of the total neutron yield through the effect on beam density, core fast ion redistribution, and indirectly through an induced decrease in critical beam energy and ion heating.

Maximum performance is achieved at 9.6 s, when the TH and BT components are approximately equal. The electron density control was not adequate in baseline D-T discharges, with core n_e increasing throughout at an approximately linear rate. This is thought to be the result of a weakening in edge-localized mode (ELM) activity, crucial for density control and impurity flushing, which lead to impurity accumulation, radiation increase and a subsequent disruption [25]. One can observe that both electron and ion temperatures start decreasing after 9.5 s, meaning that only a quasi-steady phase was reached, a consequence of a combination of the density rise and detrimental MHD activity, e.g. sawteeth and neoclassical tearing modes.

Hybrid scenario: the time interval [7.0, 10.0] s from the beginning of NBI heating to reaching flat-top performance is shown. The hybrid discharge starts at a low edge n_e at the beginning of the heating phase, with an initial deep neutral beam penetration. This results in a strong drive of T_e rise, which at low edge and core n_e (initial 500 ms) causes the collisionality to decrease. These are favourable conditions for an efficient evolution of an energetic RF tail, which contributes to both a further increase of T_e , as well as T_i . Several 100 ms into the heating phase, the ion heating is bootstrapped with the T_i increasing at a high rate of approximately 7 keV in 500 ms. The efficient triggering of the electron and ion heating channels is one of the main differences compared to the baseline scenario, with the hybrid pulse reaching levels of fusion performance close to its maximum after approximately one second, a rate twice as fast as the baseline. The hybrid TH yield rises in unison with the plasma density, which is the dominating term in the reaction rate calculation, as T_i is already high. The BT component becomes steady when both the edge electron density and temperature flatten out, equilibrating the effects of beam penetration and slowing-down time on beam density. The high performance is sustained for ~ 3 s with good core n_e control, after which the T_e profiles became hollow due to impurity accumulation, which lead to increased neoclassical tearing mode activity and performance deterioration [28]. Compared to be baseline discharge the (quasi) steady yield was dominated by the BT component, with the TH approximately 25% lower. Hybrid pulse #99950 achieved a record integral fusion energy output of 45.8 MJ for a 50-50 D-T plasma with mixed D-T beams. One can observe the benefits of an elevated- q sawtooth-free regime with no negative effects on core T_e and fast ion redistribution. Comparing the flat-top core T_e and T_i , we see that the hybrid pulses achieved ~ 1 keV larger values on average, compared to be baseline counterparts. The maximum absolute yield of the TH component is comparable in both cases.

3.2. Comparison of measured and calculated D-T neutron yield

One of the main aims of the work presented in this paper is assessing the fidelity of interpretive TRANSP calculations of the fusion power output, and comparing these to JET's absolutely calibrated neutron yield measurements. In figure 9 we present the relationship between the ratio of TRANSP

total neutron yield calculations and absolutely calibrated measurements (calculation/measurement -1 in %), and total external heating power. We compare the neutron yield discrepancy distribution for both the JET-ILW D (blue) and DTE2 (gold) discharge databases, in addition to plotting the mean of the computed ratios (bin width 5 MW). The deuterium discharge database shows good agreement between the measurements and calculations over the whole range of heating power, within the combined experimental and computational uncertainty of $\pm 25\%$ denoted with the grey dashed lines. A difference between low-power and higher performing discharges can be observed, with the heating power threshold for the grouping being around 20 MW—namely one can observe that the spread of the computed discrepancy is higher for low-power discharges with an increased mean of $\sim +15\%$ (black dashed line), while the best performing discharges, spanning a range of heating power of more than 15 MW, show an excellent agreement with measurements, with the mean discrepancy being $\lesssim +5\%$. Interestingly this finding does not agree fully with other previous studies of fusion performance modelling in deuterium plasmas on large databases [12, 13], where a systematic over-prediction of TRANSP calculations of up to $+50\%$ was reported. The DTE2 database yield discrepancy similarly exhibits a difference between plasmas heated with either above or below ~ 20 MW of power. However in D-T, calculations for discharges with relatively low power systematically over-estimate the fusion power measurements by approximately $+40\%$, while the discrepancy mean falls to around $+10\%$ for the highest performing discharges, again exhibiting a good match with the measured neutron yield. While the increased heating power mainly corresponds to high D-T performance, the Ne-seeded discharges expectedly do not follow that trend and also display uncharacteristically high yield discrepancies of around $+60\%$ [37]. The observed correlation between the calculation/measurement neutron yield discrepancy and discharge performance for both D-D and D-T plasmas is similar to the relationship observed in the analysis of fusion output contributions from different fusion components, as seen in the right-hand side graph of figure 5. Indeed if P_{heat} on the abscissa of figure 9 is replaced by the ratio between beam-induced and thermal fusion, plotted in figure 10, the discharges with larger average discrepancy cluster towards the right-hand side of the graph. This means that a majority of the pulses for which the fusion power calculation was over-predicted exhibit a beam-driven fusion performance, with a (BT+BB)/TH ratio of $\gtrsim 6$.

The DTE2 data thus suggests that the calculated beam-target fusion component might be systematically overestimated—possibly this effect is emphasized in low power discharges due to the fact that BT neutrons comprise more than 90% of the total neutron yield, and due to plasma conditions governing the behaviour of beam fast ions. The beam-induced D-T fusion rate is computed through the following two terms of equation (3): $n_{\text{db}}n_{\text{t}}\langle\sigma v\rangle_{\text{BT}}(D \rightarrow T) + n_{\text{d}}n_{\text{tb}}\langle\sigma v\rangle_{\text{BT}}(T \rightarrow D)$, which represent deuterium and tritium beams impinging on a thermal target of the opposite fuel ion, respectively. Trying to understand where the beam-target reaction rate might be overestimated, we scrutinize the terms'

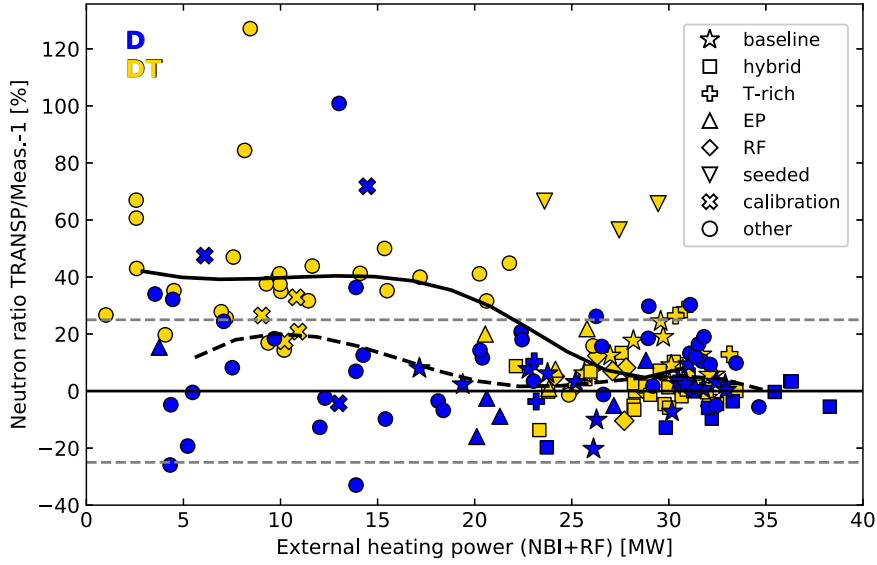


Figure 9. Comparison of the ratio between TRANSP neutron yield calculations and absolutely calibrated measurements (calculation/measurement -1 in %) for JET-ILW D (blue) and DTE2 (gold) discharge databases. The total launched NBI and RF external heating power is plotted on the x -axis. The mean of the neutron yield ratio is shown for D (black dashed curve) and D-T (black solid curve) discharges. The grey dotted lines denote a $\pm 25\%$ uncertainty of the neutron yield ratio. The scenario type legend notation is used.

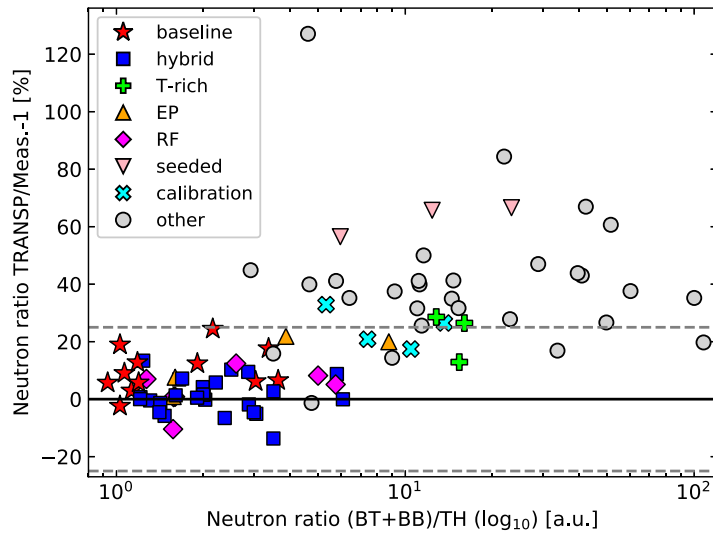


Figure 10. Ratio of TRANSP neutron yield calculations and absolutely calibrated measurements (calculation/measurement -1 in %) versus the ratio between the neutrons emitted from beam-induced and thermal fusion for the DTE2 database. The grey dotted lines denote a $\pm 25\%$ uncertainty of the neutron yield ratio. The scenario type legend notation is used.

three major dependencies: thermal ion density, beam ion density, and the beam-target reactivity. The thermal densities are relatively well defined through a combination of electron density, Z_{eff} and isotope composition measurements and are unlikely to contribute to the discrepancy, which will be expanded on in section 3.3. The beam density n_b is computed with the NUBEAM module through Monte Carlo particle tracking, however to discuss potential sources of systematic error we expand on the evolution of the beam ion population in a classical way. It is obtained by integrating the analytically or numerically obtained fast ion distribution function $f_b(E, \xi)$ in energy E and pitch angle ξ , and is related to the beam slowing-down calculation:

$$n_b \propto \int_0^{E_b} \int_{-1}^1 f_b(E, \xi) \sqrt{E} dE d\xi, \quad (4)$$

$$\text{with } f_b(E) \propto \sum_i \frac{S_i \tau_s}{\left(1 + \left(\frac{E_{\text{crit}}}{E_{b,i}}\right)^{1.5}\right)},$$

where i stands for the full, half and third-energy beam ions, S_i the beam particle source rate, τ_s the Spitzer slowing-down time, and E_{crit} the beam critical energy. The beam source term is defined by the particle deposition profiles and depends on the beam species characteristics and plasma density—these are well defined, with the shape of the deposition profiles reliable. The amplitude of the particle source on the other hand

might be affected due to beam power calibration uncertainty [16, 81], the effect of which is assessed in section 3.3. τ_s is inversely proportional to $n_e/T_e^{1.5}$ and consequently the effective collisionality. We've seen in the left-hand side graph of figure 7 that P_{fus} shows a correlation to $\langle\nu_{\text{eff}}\rangle$, with a majority of the lower performing discharges displaying higher collisionality values above ~ 5 . Additionally the slowing-down time depends on the electron Coulomb logarithm, the values of which vary by only several percent around an average of approximately 17.5 for the whole database. E_{crit} is linearly dependent on the electron temperature and is not expected to introduce significant uncertainty. To summarize, while the calculated beam density does not show a dependence on the (BT+BB)/TH yield ratio, as seen in figure 6, the beam slowing down distribution does depend on input or calculated terms that are uncertain, i.e. prescribed beam power and the computed collisionality. An additional source of uncertainty in n_b stems from the fact that NUBEAM takes into account classical and neoclassical fast ion evolution effects, but it does not describe anomalous transport, owing to turbulence and MHD activity. While this has been shown to cause computational neutron over-prediction due to a strong suppression of beam-induced fusion in the presence of resonant MHD instabilities, e.g. MAST, DIII-D and ASDEX Upgrade [82–85], it has not been unambiguously shown that similar phenomena govern the transport of fast particles in JET. Such studies have predominantly been done for deuterium-majority plasmas—for example a study of JET's 2003 trace tritium experiments in which a T beam was injected into a pure D plasma found an overestimation of the computed fusion power for both the D-D and D-T neutron dominated plasmas. To obtain a match in the neutron rates a relatively large fast ion anomalous diffusion D_a between 5 and 10 m² s⁻¹ was applied. We've applied the same level of radially-independent D_a to a selection of the D-ILW database discharges with beam-driven fusion performance, that overestimated the D-D neutron yield measurements—see D calibration scenario discharges in figure 9. It was found that at $D_a = 5$ m² s⁻¹ the beam density was significantly reduced compared to the reference case without anomalous transport— n_b was reduced by a factor of 4 in the core, while the volume-integrated value reduced by more than a factor of two. With this level of anomalous diffusion applied the n_b radial profile became extremely flat and lost all core peakedness, with the total neutron rate decreasing by around 40%. While this yield decrease compares well to the observed over-prediction, the effects of changes in beam density on calculated profiles of neutron emissivity and fast ion losses are substantial and not corroborated by diagnostics measurements. There is also no indication that MHD activity effects could exhibit a similar dependence on the external heating power as the one observed in the neutron yield discrepancy. On the contrary, the activity of fast ion driven modes like fishbones is expected to increase with rising beam power, and prominent tearing mode activity is observed in some high performing discharges. An analysis of JET's MHD activity based on measurements of a high resolution toroidal magnetic probe array published in [12], revealed no correlation between mode activity and

level of neutron yield reproduction, which is supported by our D-T observations. Namely, the low power D-T discharges with over-predicted yields shown in figure 9 have been performed with a variety of plasma conditions and combinations of external heating, e.g. NBI- and RF-only, or a combination of NBI and RF, resulting in different fast ion population characteristics. Although it has been experimentally confirmed that this induces various signatures in MHD activity and anomalous transport, e.g. due to fast ion turbulence stabilization, the spread of these discharges' computed neutron yield discrepancy around $\sim +40\%$ remains low and consistent between scenarios. The redistribution of fast ions due to sawteeth and its effect on the neutron yield have been studied at JET [86], however this is a transient effect with the sawtooth-cycle generally long enough compared to the average beam ion slowing-down time ($\lesssim 80$ ms), to allow for the fast ion distribution and neutron yield to reach a steady phase. Although we did not apply a sawtooth model in the analysis, the global effects sawteeth might have on the plasma performance, for example through core T_e collapse, are taken into account through prescribing finely time-resolved fitted profiles. The final term defining the beam-target D-T fusion yield is the reactivity $\langle\sigma v\rangle_{\text{BT}}$. The cross sections were based on the thoroughly validated Bosch–Hale parametrization [87], so the potential uncertainty lies in the relative ion velocity term—the bulk thermal ion temperature contributes relatively little to the total velocity, therefore the reactivity has a low sensitivity to uncertainty in T_i . The energy distribution of the beam ions is the term that has the largest uncertainty weight in the reactivity calculation, with the potential sources of uncertainty similar to the ones discussed for n_b . Additional investigation into the effects of MHD instabilities on the redistribution of fast ions, and consequently the beam-target neutron yield, could be made by coupling of orbit tracking and MHD codes, such as [86, 88, 89], to better describe the radially and energetically localized nature of anomalous diffusion. Experimental validation of fast ion transport at JET is difficult because the fast ion density is not measured by techniques applied at other tokamaks, e.g. the FIDA system measuring D_α light emission from neutralized fast ions [90, 91].

3.3. Computational uncertainty

To quantify the discrepancies between the calculated and measured neutron yield, the uncertainty of the TRANSP interpretively computed fusion power was calculated. This was done by varying a set of most prominent input parameters by $\pm 10\%$, i.e. the electron density, electron and ion temperature, angular rotation frequency, NBI power and the D-T thermal fuel mixture. Three representative discharges were chosen for the analysis, namely the high-performing baseline #99863 and hybrid #99950 discharges, both with slightly different fusion drivers, and the low power, neutron calibration discharge #99812, all with mixed 50-50 D-T beam injection. The latter exhibits plasma parameters representative for beam-driven fusion performance and the calculated fusion power over-estimated by an average of 25%. This discharge was

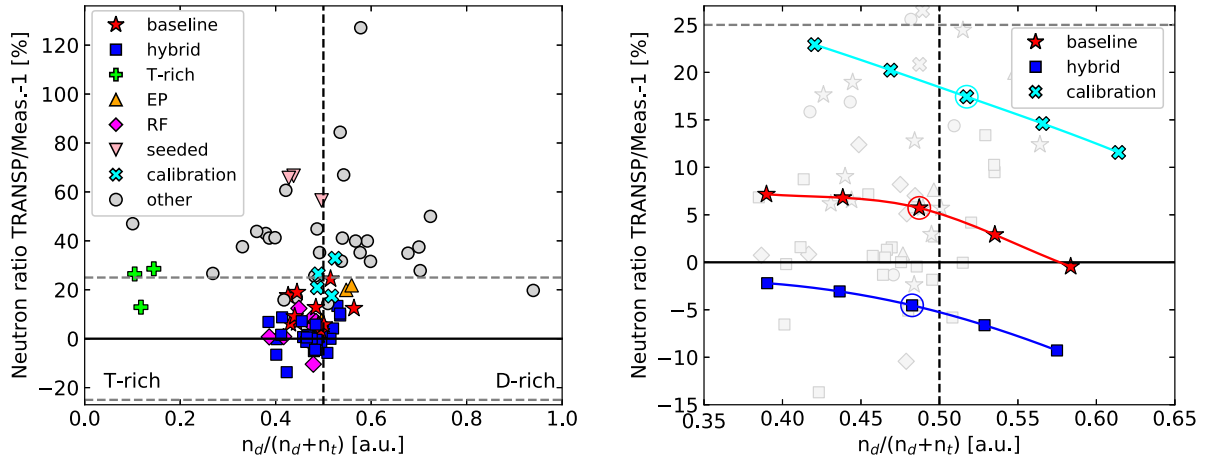


Figure 11. *Left:* ratio of TRANSP neutron yield calculations and absolutely calibrated measurements (calculation/measurement -1 in %) versus the ratio between on-axis deuterium and total fuel ion density. Deuterium-rich discharges are located on the right-hand side of the graph, with the T-rich on the left. *Right:* zoom-in of the left panel graph, displaying the fuel ratio sensitivity calculation. The fuel composition of three D-T discharges—baseline #99863, hybrid #99950 and calibration #99812—was varied by $\pm 10\%$ and $\pm 20\%$. The graphs share the scenario type legend notation.

executed for the cross-calibration of fission chambers against the time-integrated neutron yield measurements by the foil activation system [18, 92].

We first present the sensitivity study for one of the most important D-T plasma parameters, the fuel mixture—on the left-hand side graph in figure 11 the relation between the yield discrepancy ratio and on-axis $n_d/(n_d + n_t)$ is shown. Importantly, no correlation between the two can be seen, with the majority of the pulses performed within a $n_d/(n_d + n_t)$ ratio interval of $0.4 \sim 0.6$, with an approximately 5% deviation from the 50-50 mixture toward the more fusion favourable T-rich composition. As described in section 2 the initial composition of the plasma was taken from the edge residual gas analysis and extrapolated to the core, based on impurity and beam dilution. It was found that the computed core mixture matched with the fixed edge value within a couple of percent for the majority of the pulses, indicating good mixture control and fast core isotope ion mixing [29, 30, 93, 94]. The edge mixture boundary condition was varied by $\pm 10\%$ and $\pm 20\%$ for the selected discharges, in order to study the effect on the computed fusion power. The results are shown in the right-hand side panel of figure 11, where the reference TRANSP runs are encircled. One can observe all three plasma shots show a similar trend of increasing fusion power as the fuel mixture is tritiated more, and the opposite for a dominant deuterium mixture. The three scenarios show different rates of change due to their individual dependence of fusion performance on the ratio between beam-driven and thermal fusion. One can observe that with a dominating beam-target component, such as for the neutron calibration discharge, the relation between the rate of fusion power change and the fuel mixture is linear in the vicinity of the 50-50 composition. This is because the benefit of injecting deuterium beams into a T-rich plasma is significantly larger than the decreasing contribution of the thermal fusion proportional to the thermal ion density product due to a decreasing deuterium bulk concentration. On the other

hand the baseline discharge's fusion performance is dominated by thermal fusion, which means that the benefits of the D beam \rightarrow thermal T cross section is diminishing compared to the diminishing thermal density product, reaching a plateau at around $n_d/(n_d + n_t) \sim 0.4$ [30, 69]. However in all cases the relative change of the fusion power due to changes in the fuel mix is relatively small, reaching values of around $\pm 2\%$ at a 10% composition variation.

Plasma parameters input into TRANSP as fits of measured data were scaled by $\pm 10\%$, preserving gradient scale lengths (1σ uncertainty estimate due to measurement scatter and fitting). While this is a good approximation for a majority of the fits, it can be considered a lower estimate for the core ion temperature due to the scarcity of core CX measurements, which strongly depends on the plasma scenario. The nominal uncertainty of the beam power is cited as $\pm 10\%$ for both D and T beam species, according to beam calibration [16, 81]. In table 1 a summary of the sensitivity study is presented, with the variation in neutron yield dependent on the corresponding plasma parameter perturbation. In the final row the total uncorrelated uncertainty for individual scenarios is computed as $\sqrt{\sum \sigma_i^2}$. Although the assumption is made that there is no correlation between the measurements' experimental uncertainties obtained with independent diagnostics, small levels of correlation do exist, but are not considered since they will not impact the computed total uncertainty of the fusion power calculation, or the conclusions we draw on how the fusion performance relates to input uncertainty sensitivity for individual scenarios. The largest three contributors to the total computational uncertainty are denoted in bold. We can observe that n_e is an important parameter for the calculation of fusion power in both the baseline and hybrid discharges, with a 10% density change resulting in almost the same variation in the yield—in the former predominantly because the thermal fusion rate depends on the thermal ion density product. In the

Table 1. Summary of plasma parameter sensitivity study for three D-T discharges—baseline #99863, hybrid #99950 and low power neutron calibration pulse #99812—to determine the total uncorrelated uncertainty of the computed fusion power (proportional to total neutron rate R_n). Electron density n_e , electron temperature T_e , ion temperature T_i , toroidal rotation frequency Ω_t , NBI power, and D-T fuel ratio $n_d/(n_d + n_t)$ were varied by 10%, with the scaling constant being time and radius independent. The largest contributors to the total uncertainty for each discharge are denoted in bold.

Discharge → Parameter variation ↓	Baseline #99863 R_n variation (%)	Hybrid #99950 R_n variation (%)	Low power #99812 R_n variation (%)
$n_e \pm 10\%$	+9.5/−9.2	+9.9/−9.1	−0.9/+1.1
$T_e \pm 10\%$	+2.3/−3.4	+2.5/−2.7	+8.8/−9.0
$T_i \pm 10\%$	+18.0/−16.1	+14.6/−13.1	+6.8/−5.4
$\Omega_t \pm 10\%$	−1.1/+0.4	−1.1/+0.9	−1.3/+1.5
$P_{\text{NBI}} \pm 10\%$	+14.2/−13.2	+15.5/−13.6	+33.7/−28.2
$n_d/(n_d + n_t) \pm 10\%$	−2.7/+1.0	−2.2/+1.5	−2.4/+2.4
Uncorrelated total uncertainty	+25/−23	+24/−21	+36/−30

hybrid discharge this is due to a combination of an effect on the thermal density, playing a role in both thermal and, linearly, in beam-target fusion, as well as beam penetration. The neutron calibration discharge shows a weak sensitivity to variations in n_e , a consequence of the fusion performance being driven by the beam-target component. Namely the linear relation between the BT fusion rate and thermal ion density is countered by the beneficial effect of improved beam penetration, higher core beam density and longer beam slowing-down times, boosting the fusion reactivity. The variation in T_e shows little effect on the baseline and hybrid discharges because the core T_e values are already relatively high, as shown in figure 8, with the $\sim 2.5\%$ R_n change due to beam-slowing down. Again, owing to the beam-target dominance the variation of T_e in low power discharges, such as the neutron calibration discharge, will trigger changes to the beam slowing-down dynamics through collisionality, indicated in equation (4), resulting in changes of the total R_n of $\pm 9\%$. The largest effect on baseline's fusion output is triggered by perturbing T_i , reaching a maximum of 18% due to its strong dependence the TH yield. The impact on the hybrid performance is similarly high at just below 15%, while the neutron calibration discharges show a weaker response at around half the values of the other scenarios, mostly stemming from the effect on the computed $\langle \sigma v \rangle_{\text{BT}}$ reactivity for the low energy part of the beam ion distribution. The perturbation of plasma rotation input does not propagate to large discrepancies in R_n , with an average scenario-independent value of around 1%. The uncertainty of the beam power on the other hand has a large effect on the total yield calculation—since this is an interpretive analysis the change in beam power will not propagate to kinetic profiles, and will thus only enter the fusion power calculation through the beam source strength term, illustrated with equation (4), affecting the BT and BB components. Baseline and hybrid discharges record an approximately 15% change in the total yield, rivalling the importance of T_i , while the effect on the neutron calibration discharge is extremely large. In the latter, the $\sim \pm 30\%$ change originates from the effects on the evolved beam ion density profile, which is similar for the reference and perturbed cases within $\rho = [0.7, 1.0]$, but it starts to deviate

towards the plasma core reaching a difference of 25%–30% on-axis. Additionally, we have varied the impurity composition of the baseline case from the original 1% Be, 0.01% Ni and 0.48% Ne—a variation of ± 0.75 was applied only to beryllium, because it is the dominant core impurity dilutant. The resulting effect on the quasi-neutrality and Z_{eff} calculation was absorbed by Ne, the concentration of which changed by $\mp 0.1\%$. The core dilution change resulted in a total yield variation of around $\pm 3.5\%$, which is expected to be equivalent in the hybrid case due to a similar response to n_e perturbation, and small for the neutron calibration discharge. Summing up the contributions yields, a total computational uncertainty estimate for the fusion power of approximately 25% for the baseline and hybrid, and 35% for the low-power neutron calibration discharges is found. This shows that the uncertainty of D-T neutron yield calculations based on validated data is much larger than the experimental uncertainty of the absolute neutron yield measurements, estimated to be below $\lesssim 10\%$ [7]. In addition, the calculational uncertainty is found to be dependent on the mechanisms driving fusion performance, and thus the characteristics of individual plasma scenarios.

3.4. Fusion alpha power calculations

We briefly report on an important physics insight of JET's DTE2 experiments, calculations of the fusion alpha power. Because the fusion alpha source strength is linearly proportional to the neutron yield, the fidelity of alpha particle effects modelling is related to our capability to reproduce the measured fusion performance. Having validated the computed neutron yield, we can analyse the trends of alpha power balance computed by TRANSP, and assess the alpha pressure—both of these quantities are relevant for extrapolation of conditions to burning plasmas of future fusion reactors, where we will need to understand the role alphas play in plasma self-heating and in driving plasma instabilities such as Alfvén eigenmodes. In the left-hand side panel of figure 12 we present the relationship between the alpha heating power and the external plasma heating power. The power balance is split into the electron (blue) and ion (red) channels, both exhibiting a power-law relation

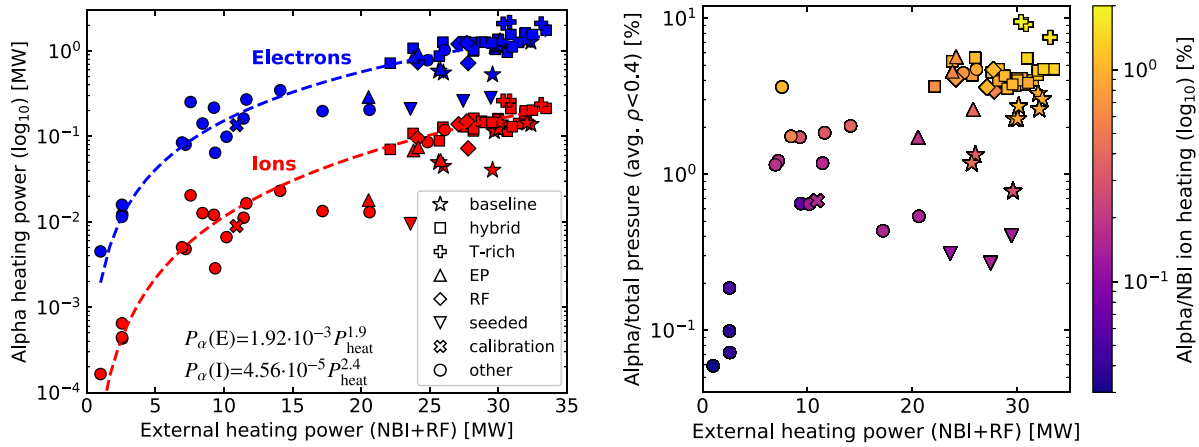


Figure 12. *Left:* alpha heating power to the electron (blue) and ion (red) channels versus the launched external NBI and RF heating power for the DTE2 database. The alpha heating rise rate is fitted with a power-law function. *Right:* computed ratio between the alpha and total ion pressure in the plasma core (averaged over $\rho < 0.4$) versus the launched external NBI and RF heating power. The z -axis (colourbar) denotes the ratio between the total alpha and NBI ion heating. The graphs share the scenario type legend notation.

to the increasing heating power, correlated to the P_{fus} trend shown in figure 3. One can observe that for maximum achieved values of P_{heat} above 30 MW the alpha heating of electrons reached levels of around 1–2 MW, while the ion heating was computed to reach up to 200–300 kW. The computed exponents of the $P_{\text{heat}}^{\lambda}$ power-law fit are $\lambda(\alpha_e) = 1.9 \pm 0.4$ for electrons, and $\lambda(\alpha_i) = 2.4 \pm 0.5$ for ions, with the ratio between electron and ion heating from alphas being $\lesssim 10$ for the high performing discharges and decreasing (generally independent of the deviation of individual discharges from the power-law fit). On the right-hand side graph of figure 12 we plot the relative contribution of the alphas to the total pressure in the core (averaged within $\rho < 0.4$) versus P_{heat} . The alpha pressure was computed using the alpha density and effective temperature obtained through NUBEAM Monte Carlo particle tracking. For an alpha energy distribution slowed-down from 3.5 MeV birth energy, the average energy of alpha particles in the core varies between 0.9 and 1 MeV. One can observe that the cluster of high performing pulses recorded relative alpha pressure levels of around 3%–5%, while the T-rich achieved the highest relative contribution of $\sim 10\%$. The core-averaged slowing-down time of the alpha particles varied between 100 ~ 640 ms, depending on plasma density and temperature, and had an average value of 330 ms for the D-T database. On the z -axis we additionally plot the ratio between the total alpha and beam ion heating. It can be seen that there is a strong and favourable increase in the relative contribution of alphas to the ion heating, however for the highest performing T-rich discharges, with the largest alpha source strength, it is still limited to just below 2% relative to the beams. The relative alpha ion heating rise rate is approximately half an order of magnitude per 10 MW of additional heating.

Plasma heating in future fusion reactors is expected to largely affect the electron channel because systems aimed at electron cyclotron heating will be heavily relied on, negative beam ion injection systems are planned to be used, and because dominant alpha self-heating conditions are expected to be achieved, with a predominant direct contribution to

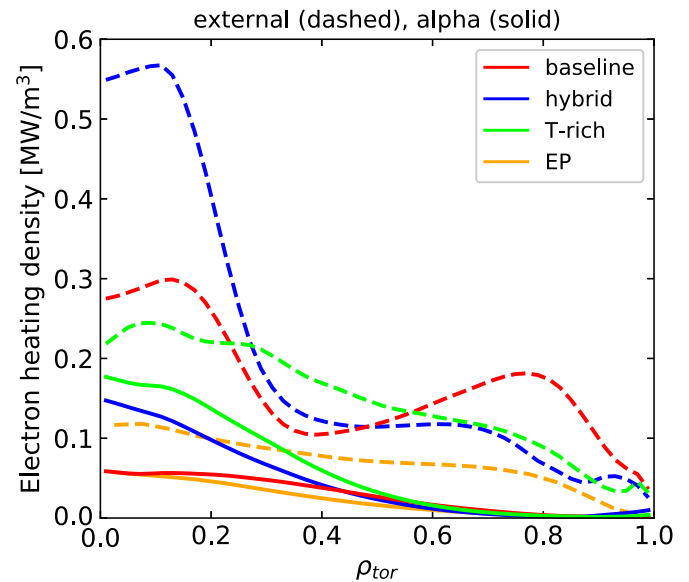


Figure 13. Comparison of the computed external (dashed—NBI+RF+Ohmic) and alpha (solid) electron heating power density profiles for a selection of best performing DTE2 discharges (baseline #99948, hybrid #99912, T-rich #99965 and EP #99802).

the electron power balance. In figure 13 we show a comparison between the computed electron heating density profiles stemming from external sources (sum of NBI, RF and Ohmic heating), and alphas. The comparison is shown for individual DTE2 scenarios for selected high performing shots (a subset of discharges shown in figure 4: baseline #99948, hybrid #99912, T-rich #99965 and EP #99802). One can observe that in contrast to the ion heating, alphas contribute to the electron heating at a level comparable with that of combined external heating sources. Both the baseline and hybrid discharges have a double-humped shape of external electron heating profile. This arises as a combination of beam power deposition dominating from $\rho > 0.4$ to the separatrix, more pronounced in the

baseline case due to lower penetration at higher plasma density, and RF heating profile that peaks in the vicinity of the magnetic axis, within $\rho \lesssim 0.2$. The ratio of alpha over external electron heating, averaged within $\rho \leq 0.1$, is 0.20 for the baseline and 0.25 for the hybrid discharge. The EP hybrid-like discharges do not employ RF heating, therefore their external heating profile is determined by beam penetration at low electron densities, hence the core peakedness. The ratio of alpha over external electron heating in the core is 0.46. The highest absolute and relative contribution of alpha electron heating was computed for the record performing T-rich discharges. In these discharges the external heating profile has a relatively low peakedness due to the dominating beam heating over RF, with a high ratio of alpha over external electron heating in the core of 0.72. Because the alpha source term is linked to fusion reactivity, all the computed alpha heating profiles can be observed to peak on the magnetic axis. Although the volume-integrated contribution of the core alpha heating to the global power balance is modest, conditions in which the alpha electron heating is comparable to the sum of external electron heating sources was achieved locally in the highest performing D-T discharges.

4. TRANSP fusion yield modelling of fundamental RF heating of a large minority

In this section we report on the TRANSP modelling workflow developed to accurately calculate the fusion yield in discharges employing the fundamental RF heating of a large minority. This posed the biggest challenge in interpretive TRANSP modelling of fusion performance for the DTE2 database, and was applicable to the record T-rich scenario. We analyse a representative T-rich pulse #99972, performed at a fuel mixture of 10:90 D-T, on-axis magnetic field of $B_0 = 3.85$ T, plasma current of $I_p = 2.5$ MA, with approximately 29 MW of deuterium NBI heating. In addition ~ 3.7 MW of ICRH power was applied at a frequency of $\nu_{RF} = 29$ MHz, adjusted for on-axis $N = 1$ deuterium heating [30, 34]. In this heating configuration the Maxwellian distribution of the bulk D ions is accelerated by the RF interaction and forms an energetic tail, extending to energies above several hundred keV. In addition there is a synergy effect between the RF waves and the fast beam deuteron population, via the Doppler shifted resonance, however it is not as prominent as when employing the second harmonic RF scheme. TRANSP can describe the latter effect with the quasi-linear RF kick operator [43, 44], which enables the communication of TORIC computed quantities to NUBEAM, e.g. the RF electric field components and perpendicular wave vector for each toroidal mode, and has been validated at JET [18, 45]. However TRANSP cannot fully model the absorption of RF power on bulk thermal species ($< 1.5T_i$) and requires defining a dedicated fast RF minority species, with concentrations typically between 0.5% and 5%. While the TRANSP native FPP code solves the bounce-averaged Fokker–Planck equation to compute the fast ion distribution function $f_{RF}(E, \mu, r, t)$ —as a function of energy E , magnetic moment μ (or equivalently pitch angle ξ), minor

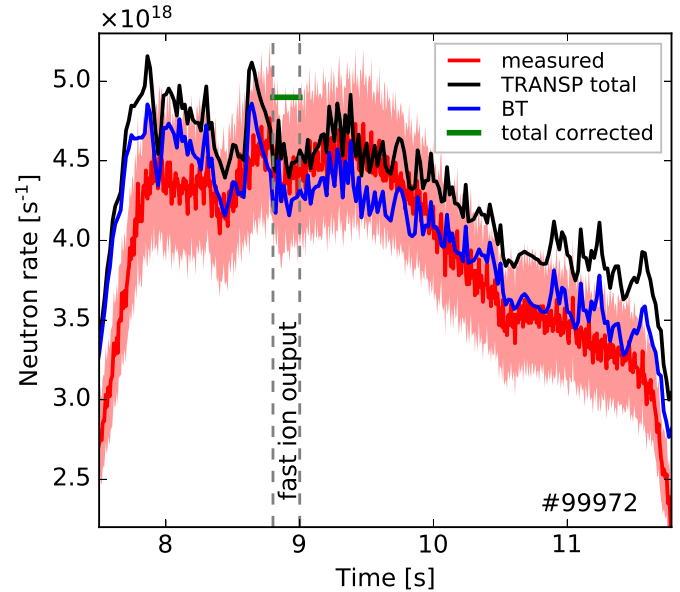


Figure 14. Comparison of the measured (red) and TRANSP computed (black) neutron rates for the T-rich D-T discharge #99972, including the beam-target component (blue) and the corrected calculation of total rate including the contribution of RF-accelerated deuterium-bulk tail (green). The grey dashed lines denote the 0.2 s time interval over which the fast ion distribution functions were averaged. The $\pm 10\%$ experimental uncertainty is denoted with the red shaded band.

radius r and time t —it does not have a self-collisional operator, does not communicate the RF-tail collisional term to TRANSP, assumes the background species are Maxwellian, and does not communicate the fusion output contribution to the total yield calculation [95]. Additionally the beam-slowing down calculation is not done in consistency with the RF minority definition, with NUBEAM disregarding the RF minority density. Therefore if the RF-accelerated thermal ions are fuel particles contributing to the total yield, and the RF species density is too large to be a minority, i.e. $\gtrsim 5\%$, an alternative modelling workflow needs to be found in order to accurately describe the heating effects.

We've solved this with the following procedure: (i) running a reference calculation in which the $\sim 10\%$ bulk deuterium is considered to be a completely thermal species. This facilitates a consistent beam slowing-down calculation, providing an estimate of the beam-induced fusion contribution, including D beam-T thermal and D beam-D beam fusion, including the effects of NBI+RF synergy. (ii) Running a repeat simulation in which the bulk deuterium is fully defined as an RF minority species, explicitly bypassing TRANSP's flag for using the same beam and RF isotope, in order to evolve it wholly as a Maxwellian with an energetic tail with FPP. The f_{RF} distribution function is averaged over a specified time interval. (iii) Extracting the RF distribution function and using it to calculate the contribution of the deuteron Maxwellian and tail to the total fusion power. The first-step simulation results are shown in figure 14, where we display the comparison between time-resolved measurements (red) and calculations (black) of the total neutron yield. One can observe a good match both in

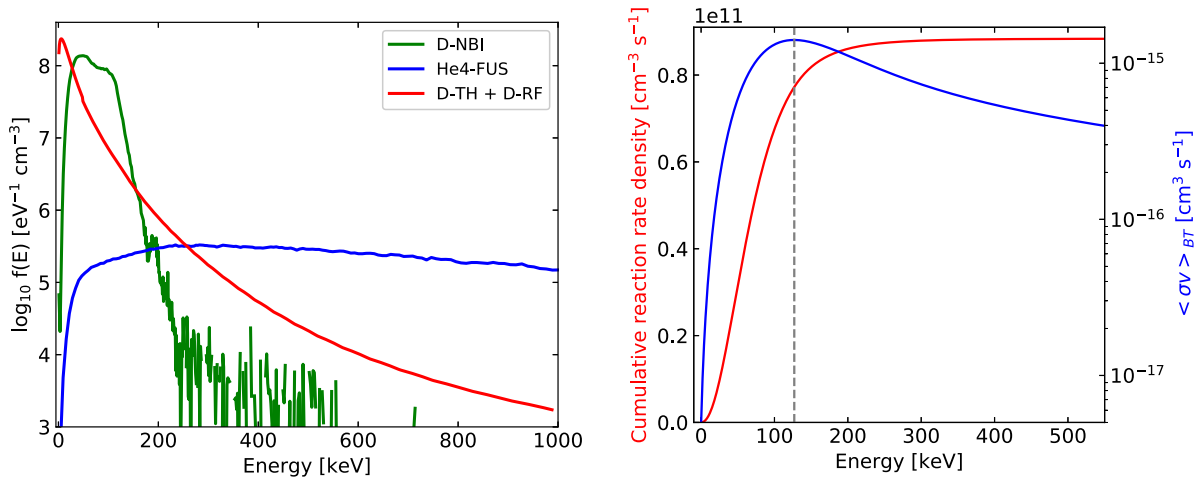


Figure 15. *Left:* calculated core ion energy distribution functions for the T-rich D-T discharge #99972, including the deuterium fast beam ion distribution (green), fusion alpha distribution (blue, extends up to ~ 3.5 MeV), and the RF-accelerated deuterium-bulk tail distribution (red). *Right:* computed core cumulative reaction rate density (red, left y-axis) and the deuterium beam \rightarrow thermal T reactivity $\langle \sigma v \rangle_{BT}$ (blue, right y-axis), dependent on fast ion energy. The grey line denotes the ion energy at which the maximum reactivity is reached.

the absolute values and the relative shape of the yield time evolution, especially in the highest performing part of the discharge. One can observe that the performance is predominantly beam-target driven (blue), with approximately 7%–8% computed to be the thermal contribution, omitting the RF D-bulk heating. The beam-target calculation does not include the D-RF tail contribution, but the latter is insignificant due to the low yield of the missing D beam \rightarrow D-RF fusion. The BB component is very low due to the same reason. In the second-step simulation we chose to output f_{RF} in the interval of [8.8, 9.0] s, denoted with the dashed grey lines in figure 14. The RF power balance, including the D-RF minority, shows that approximately 10% of the power is absorbed by the electrons, with the rest equally split between absorption on the D-bulk and D-beam ions, meaning that around 45% of RF power will be pumped into energizing the bulk Maxwellian deuterons. There is RF power absorption on fusion alphas, but is negligible and amounts to around 20 kW.

The TRANSP-FPP computed bounce-averaged Fokker-Planck RF distribution function f is defined such that the average minority particle density within a flux-surface averaged zone in (E, ξ) coordinates is given by [95]:

$$\langle n \rangle = \frac{4\pi}{m^2 B_0} \int dl/B \int_0^\infty dE \int_{-1}^1 f \tau_B |\xi| E d\xi, \quad (5)$$

where m is the particle mass, B_0 the minimum magnetic field along a field line, and τ_B the average orbit bounce time. Using the computed bounce-average integrals from equation (5) the distribution function is normalized and integrated over the pitch angle to obtain the energy dependent function f_{RF} . We plot the core ($\rho = 0.025$) f_{RF} (red) in the left-hand side panel of figure 15, together with the D-beam (green) and fusion alpha (blue) energy distribution functions evolved by NUBEAM. One can observe that the slowed-down beam distribution has a characteristic full-half-third energy structure, with the max source energy of 100 keV, in addition to a modest synergy

tail visible as an extension beyond ~ 180 keV. The low-energy part of the alpha distribution continuum can be seen, which extends up to its fusion birth energy of ~ 3.5 MeV. The calculated RF-accelerated D-bulk distribution exhibits a thermal Maxwellian shape with an exponentially decaying tail. Although the distribution extends to energies of 1 MeV, the density drops by more than two orders of magnitude compared to the Maxwellian bulk at 200 keV, and another order of magnitude by 300 keV when its concentration is lower than that of the alpha particles. f_{RF} is input into the fusion rate calculator, in which we use the beam-target fusion reactivity, plotted in the right-hand side graph of figure 15 (blue). The reactivity shows a clear peaked shape, reaching its maximum value at 127 keV (core $T_i = 9.8$ keV). We additionally plot the energy dependence of the cumulative reaction rate density, including the D-minority and T-thermal density distributions. It can be seen that 88% of the total fusion rate is contributed by RF-accelerated deuterons below the energy of $\langle \sigma v \rangle_{BT}$ peak, while at 200 keV 98% of the total fusion contribution is accounted for. Radially outward from the magnetic axis the RF-tail decays quickly with 90% of the total D-bulk contribution to the fusion power reached at $\rho \sim 0.4$. The corrected total fusion power in #99972 is computed as a sum of the BT and BB components from the original run, and the TH with an RF-tail contribution from the RF-minority run. We assess that approximately 4%–5% of the total neutron yield stems from Maxwellian fusion, while an additional 10% is computed to result from the RF-accelerated D-bulk tail. This is in line with neutron spectrometer observations and alternative calculations reported in [30, 34]. The TRANSP corrected total neutron rate, averaged over the fast ion distribution output interval, is shown in figure 14 with the green bar. A 10% increase to the originally calculated TRANSP neutron yield is applied to the other two T-rich modelled discharges as well throughout this paper. It is partly due to this modelling correction, that the T-rich discharges display an over-predicted TRANSP neutron yield seen in figure 10, which is in line with observations for

the calculated P_{fus} of other discharges with dominating beam-target fusion, albeit at much lower external heating power.

5. Discussion and conclusions

New deuterium-tritium plasma experiments have been performed at JET with a Be/W wall more than 20 years after DTE1. Significant progress has been made in the understanding of tokamak physics, development of plasma modelling workflows, and improvement of JET's diagnostics systems [22, 23]. In this period TRANSP has been continuously used to support JET's experimental and scientific program, predominantly through interpretive plasma analyses, inter-shot control room support, and predictive modelling. Substantial work has been done on building and verifying improved TRANSP modelling frameworks and promotion of rigorous data validation at JET [41, 55]. Additionally, significant effort was invested into validating TRANSP's synthetic diagnostics and fast ion output against experiments, e.g. the NBI and NBI+RF synergy fast ion distribution function calculations [15, 77, 96, 97], and study of fusion products and their effects on diagnostics [18, 98–100]. The compilation of a database of reliable D and D-T interpretive TRANSP runs is largely owed to a JET-wide continuous investment into the improvement of diagnostics data validation and processing, modelling framework development, and unification of modellers' assumption and techniques. In this paper we present an overview of D-T fusion performance interpretive modelling using TRANSP and its heating modules. We focus on describing the general trends observed across a wide range of JET DTE2 plasma operational parameters, such as the performance driving mechanisms, neutron yield component contributions, computational uncertainty dependencies, and fusion alpha power. Below we summarize the main observations of the paper, insightful for further D-T modelling and extrapolation to ITER and future fusion devices, and highlight the most pressing modelling questions that remain to be answered.

We find that interpretive simulations confirm a general power-law relationship between increasing external heating power and fusion output, which is supported by absolutely calibrated neutron yield measurements. It is shown that although the beam-induced fusion generally dominates the D-T performance over a ~ 35 MW range of P_{heat} , the thermal fusion component is strongly increasing with rising power, with the ratio of BT/TH decreasing with a weak power-law dependence on P_{fus} . The thermal component maximization effort culminated in a set of baseline scenario discharges that have displayed a sustained BT/TH ratio of $\lesssim 1$. The thermal fusion component rise correlates well with an increasing trend in total ion heating, resulting in a favourable decoupling of ion and electron temperatures at higher external heating power. It is shown that a majority of the highest performing discharges operated at relatively low collisionalities and high plasma rotation, both positively affecting the fusion performance through enabling good beam penetration and evolution of energetic RF-minority tails, and suppression of turbulence by increased rotational shear.

The addition of RF heating is shown to have a clear positive impact on the fusion performance, both through direct induction of fusion reactions by fuel ion acceleration, or indirectly through driving an increase in T_e and T_i . TRANSP calculations show that in JET DTE2 plasmas alphas contribute up to an additional ~ 2 MW to the plasma heating, but the majority of the power is coupled to the electron channel. A comparison of fusion performance between two high-power baseline and hybrid discharges shows that in the hybrid scenario significant electron and ion heating was established early in the heating phase, at a rate twice as high as the baseline—however the hybrid fusion performance remains dominated by beam-induced fusion reactions. The baseline discharges suffered from detrimental effects of uncontrolled n_e increase on performance, but indicate a thermal fusion dominated discharge pathway, provided D-T plasma control issues can be overcome. Note that the conclusions we draw about the approach of both baseline and hybrid discharges' conditions to a thermal fusion dominated performance are relevant for JET's heating configuration and transport conditions, yet remain relevant for informing extrapolations to ITER operations in D-T [25, 28].

One of the main aims of the paper was to assess our capability of computationally reproducing the fusion performance of various D-T plasma scenarios using different external heating and fuel mixture configurations, summarized in figure 9. Two unexpected observations are reported—that fusion power calculations for the equivalent D-ILW plasma database, of similar sample size and plasma parameters phase-space compared to DTE2, exhibit good agreement with the measurements across the whole range of P_{heat} . While an increase in deviation for beam-target driven lower-performing D shots can be seen, it is unsystematic and below the estimated uncertainty. This is in contrast to the systematic over-prediction of calculations of up to 50% reported in previous studies, albeit dealing predominantly with discharges performed with JET's carbon wall [12, 13]. We postulate that a better agreement was achieved in this work through a combination of favourable diagnostics and modelling improvements. These are the systematic increase in absolute values of D-D neutron yield measurements of $\sim +14\%$, applied to discharges performed after 2013 (improved by the use of newer standard dosimetry libraries for the neutron activation system [101]), the availability of CX measurements providing T_i and Ω_i profiles ($T_i = T_e$ was frequently assumed in previous work [74]), the application of the iterated pressure-constrained EFIT++ equilibrium reconstruction procedure [55] (which can significantly affect the neutron rate due to its effect on the Shafranov shift), and overall more consistency in modelling assumptions, e.g. fitting routines, heating settings, impurity composition. A comparison of measured and computed JET D-T neutron rates shows that the calculations' discrepancy depends on the absolute neutron yield. The calculations are found to agree well with measurements for higher performing discharges with external heating power above ~ 20 MW, while low-neutron shots display an average discrepancy of around $+40\%$ compared to measured neutron yields. A similar trend is found

for the ratio between thermal and beam-target fusion components, where larger discrepancies are on average seen in shots with dominant beam-driven performance. A targeted analysis in support of beam calibration has found that there are differences in the performance of individual beam lines at similar nominal power, resulting in difficulties in matching the TRANSP computed neutron yield and plasma stored energy to measurements. In addition a dependence of the D-T yield calculation over-prediction on the beam species was found, presented in detail in [81]. Similarly to our analyses, these findings indicate that the beam source term or anomalous beam ion transport might contribute to the observed discrepancy, through uncertainty in beam calibration affecting plasmas with only D or mixed D-T beams differently, and the contribution of MHD activity to anomalous diffusion. It is highly likely that these two processes contribute in a combined way in decreasing the beam ion density and altering their energy distribution function, agreeing with the observation that the BT component is over-estimated. It is important to emphasize that input D and D-T plasma parameters were not adjusted in the modelling to improve the match between the measured and calculated neutron yield, in order to assure comparability of results. A cross-code benchmark study against NUBEAM-equivalent beam slowing-down codes, such as ASCOT [102], LOCUST [88] or RABBIT [83], is proposed for future work, predominantly aimed at validating the beam slowing-down calculation in D-T plasmas across a range of fusion performance, using identical equilibrium and kinetic profile inputs as in the presented database. A comparison between NUBEAM and ASCOT was done for D plasmas, where the beam-target fusion component was found to be larger in NUBEAM, while the thermal and beam-beam component were consistent [75]. However due to the fact that significant differences were found in the equilibrium and profile fits used in the two codes, the observed systematic difference in the BT fusion of this study is not conclusive. Additional studies into the effect of fast ion redistribution due to MHD activity for JET D-T scenarios are proposed for future work, specifically aimed at core localised modes using state-of-the-art workflows coupling orbit tracking and MHD codes [86, 88, 89].

An assessment of the fusion power computational uncertainty due to uncertainty in the input data shows a strong dependence on the plasma scenario type and fusion drive characteristics. The combined uncorrelated uncertainty varies from approximately $\pm 25\%$ for the high-performing baseline and hybrid discharges, to $\sim \pm 35\%$ for the neutron calibration discharges, representative of low power highly BT-fusion driven plasmas. It is worth noting that although the mean calculated yield discrepancy for the low-power D-T discharges is relatively large at $+40\%$ compared to the measurements, the estimated computational uncertainty for discharges with dominating beam-induced fusion is of similar value. Appreciating the magnitude of these uncertainties—it is sobering that a fusion power calculation accurate within $\pm 25\%$ – 35% is the optimal result, obtained with significant investment into data validation and improvement of modelling workflows. This indicates the need for a more consistent and

rigorous approach to minimizing measurement and computational uncertainty, and implementing uncertainty quantification in tokamak physics. The results imply that predictive JET D-T simulations and extrapolations to D-T plasmas in future fusion reactors can expect similar uncertainty levels for the estimated fusion power output, when based on existing experimental data [11].

TRANSP computes the maximum total alpha heating power to be of the order of 2 MW for the best performing pulses in DTE2, with approximately 90% of the power flowing into the electron channel. The ratio between alpha electron and ion heating was found to be $\lesssim 10$ for the majority of the discharges, but is decreasing with a dependence of $\sim \sqrt{P_{\text{heat}}}^{-1}$. The alpha ion heating power reached a maximum of 2% with respect to that provided by beam injection, with the alpha contribution to the total pressure peaking at just below 10%. The computed alpha distribution functions are used as input in further studies, investigating experimental proof of alpha heating and alpha drive of instabilities such as Alfvén eigenmodes [32, 36, 103–105]. It was found that conditions in which the alpha electron heating is comparable to the sum of external electron heating sources were achieved locally in the highest performing D-T discharges, with the alpha over external electron heating ratio of ~ 0.7 in the core of T-rich shots.

We additionally show that the highest performing pulses in the DTE2 campaign, part of the hybrid-like T-rich scenario, cannot be modelled fully by TRANSP by default because the fundamental RF heating scheme was applied, aimed at D-bulk ions representing a large minority. Adopting a modified modelling workflow, we show that the contribution of the deuteron Maxwellian distribution with an energetic RF tail to the total fusion yield is approximately 15%. The TRANSP FPP module, providing a quasi-consistent calculation of the effect of RF power deposition on a large minority thermal ion species, is superseded by higher fidelity codes such as CQL3D [106] and FOPLA [34]—in the future we plan on benchmarking the computed distribution functions against these codes. These are also planned to be used to support the TRANSP analyses of similarly complex DTE2 RF heating experiments, e.g. second harmonic D and T heating [35], and the three-ion T-(^9Be)-D scheme [77, 107].

To summarize, with a coordinated modelling effort based on rigorously validated diagnostics data, consistent modelling techniques, and improved workflows we have compiled a database of JET DTE2 TRANSP interpretive simulations. The database includes a broad spectrum of plasma scenarios with varying machine and plasma parameters, highlighting different fusion performance characteristics. We have shown that for a majority of the database a good match between measurements and calculations of global consistency check parameters is obtained, within the estimated uncertainties. Most importantly, it is shown that the calculated fusion power for the highest performing discharges of JET's D-T campaign with a Be/W wall is in excellent agreement with the absolutely calibrated 14 MeV neutron yield measurements. This forms a reliable scientific foundation to underpin our understanding of JET's fusion performance in

the D-T campaign, and provides validated input for extensive synthetic diagnostics benchmarking, D-T predictive modelling and code development [11, 68].

Acknowledgments

This work has been carried out within the framework of the EUROfusion Consortium, funded by the European Union via the Euratom Research and Training Programme (Grant Agreement No. 101052200—EUROfusion). Views and opinions expressed are however those of the author(s) only and do not necessarily reflect those of the European Union or the European Commission. Neither the European Union nor the European Commission can be held responsible for them. This work has been part-funded by the EPSRC Energy Programme with grant number EP/W006839/1.

The Barcelona Supercomputing Center part of this work has contributed through the Spanish National R&D Project PID2019-110854RB-I00 funded through MCIN/AEI/10.13039/501100011033. In addition BSC are grateful for the support received from the Departament de Recerca i Universitats de la Generalitat de Catalunya via the Research Group Fusion Group with code: 2021 SGR 00908.

The Laboratorio Nacional de Fusión contribution was funded in part via the Spanish National R&D Project PID2021-127727OB-I00 funded through MCIN/AEI/10.13039/501100011033.

ORCID iDs

Ž. Štancar  <https://orcid.org/0000-0002-9608-280X>
 K.K. Kirov  <https://orcid.org/0000-0001-8104-4782>
 F. Auriemma  <https://orcid.org/0000-0002-1043-1563>
 H.-T. Kim  <https://orcid.org/0009-0008-2549-5624>
 M. Poradziński  <https://orcid.org/0000-0002-1858-4046>
 R. Lorenzini  <https://orcid.org/0000-0001-8353-4857>
 M. Gorelenkova  <https://orcid.org/0000-0001-8487-1396>
 F. Poli  <https://orcid.org/0000-0003-3959-4371>
 A. Boboc  <https://orcid.org/0000-0001-8841-3309>
 S. Brezinsek  <https://orcid.org/0000-0002-7213-3326>
 F.J. Casson  <https://orcid.org/0000-0001-5371-5876>
 D. Van Eester  <https://orcid.org/0000-0002-4284-3992>
 J.M. Fontdecaba  <https://orcid.org/0000-0001-7678-0240>
 D. Gallart  <https://orcid.org/0000-0003-1663-3550>
 J. Garcia  <https://orcid.org/0000-0003-0900-5564>
 L. Garzotti  <https://orcid.org/0000-0002-3796-9814>
 A. Kappatou  <https://orcid.org/0000-0003-3341-1909>
 V.G. Kiptily  <https://orcid.org/0000-0002-6191-7280>
 D. Kos  <https://orcid.org/0000-0002-9550-4329>
 C.F. Maggi  <https://orcid.org/0000-0001-7208-2613>
 P. Mantica  <https://orcid.org/0000-0001-5939-5244>
 M. Maslov  <https://orcid.org/0000-0001-8392-4644>
 M. Nocente  <https://orcid.org/0000-0003-0170-5275>
 H.J.C. Oliver  <https://orcid.org/0000-0002-7302-085X>
 S.E. Sharapov  <https://orcid.org/0000-0001-7006-4876>
 E.R. Solano  <https://orcid.org/0000-0002-4815-3407>
 H.J. Sun  <https://orcid.org/0000-0003-0880-0013>

References

- [1] Breslau J., Gorelenkova M., Poli F., Sachdev J., Pankin A., Perumpilly G., Yuan X. and Glant L. 2018 *TRANSP* (Princeton Plasma Physics Laboratory (PPPL), USDOE Office of Science (SC), Fusion Energy Sciences (FES) (SC-24)) (<https://doi.org/10.11578/dc.20180627.4>)
- [2] Goldston R.J., McCune D.C., Towner H.H., Davis S.L., Hawryluk R.J. and Schmidt G.L. 1981 New techniques for calculating heat and particle source rates due to neutral beam injection in axisymmetric tokamaks *J. Comput. Phys.* **43** 61–78
- [3] Ongena J.P.H.E., Voitsekovich I., Evrard M. and McCune D. 2012 *Numerical Transport Codes, Fusion Science and Technology* **61** 180–9
- [4] Batistoni P. et al 2018 14 MeV calibration of JET neutron detectors—phase 1: calibration and characterization of the neutron source *Nucl. Fusion* **58** 026012
- [5] Batistoni P. et al 2018 14 MeV calibration of JET neutron detectors—phase 2: in-vessel calibration *Nucl. Fusion* **58** 106016
- [6] Čufar A. et al 2018 Calculations to support *in situ* neutron yield calibrations at the Joint European Torus *Fusion Sci. Technol.* **74** 1–17
- [7] Batistoni P., Popovichev S., Conroy S., Lengar I., Čufar A., Abhangi M., Snoj L. and Horton L. 2017 Calibration of neutron detectors on the Joint European Torus *Rev. Sci. Instrum.* **88** 103505
- [8] Štancar Ž., Gorelenkova M., Conroy S., Sauvan P., Buchanan J., Weisen H. and Snoj L. (JET Contributors) 2019 Multiphysics approach to plasma neutron source modelling at the JET tokamak *Nucl. Fusion* **59** 096020
- [9] Juarez R. et al 2021 A full and heterogeneous model of the ITER tokamak for comprehensive nuclear analyses *Nat. Energy* **6** 150–7
- [10] Garcia J., Challis C., Gallart D., Garzotti L., Görler T., King D. and Mantsinen M. 2017 Challenges in the extrapolation from DD to DT plasmas: experimental analysis and theory based predictions for JET-DT *Plasma Phys. Control. Fusion* **59** 014023
- [11] Kim H.-T. et al 2023 Validation of DT fusion power prediction capability against 2021 JET D-T experiments *Nucl. Fusion* **63** 112004
- [12] Weisen H. et al 2017 The ‘neutron deficit’ in the JET tokamak *Nucl. Fusion* **57** 076029
- [13] Baranov Y.F. et al 2009 Anomalous and classical neutral beam fast ion diffusion on JET *Plasma Phys. Control. Fusion* **51** 044004
- [14] Kim H.-T., Sips A., Challis C., Keeling D., King D., Joffrin E., Szepesi G., Buchanan J., Horton L.D. and Yuan X. 2020 1997 JET DT experiments revisited—comparative analysis of DD and DT stationary baseline discharges *Nucl. Fusion* **60** 066003
- [15] Kirov K. et al 2021 Analysis of the fusion performance, beam–target neutrons and synergistic effects of JET’s high-performance pulses *Nucl. Fusion* **61** 046017
- [16] King D.B. et al 2018 Neutral beam injection on JET: effect on neutron discrepancy and energy balance *45th EPS Plasma Physics Conf. (Prague, Czech Republic, 2–6 July)* p P4.1067 (available at: <http://ocs.ciemat.es/EPS2018PAP/pdf/P4.1067.pdf>)
- [17] Sirén P., Varje J., Weisen H. and Giacomelli L. 2019 Role of JETPEAK database in validation of synthetic neutron camera diagnostics and ASCOT- AFSI fast particle and fusion product calculation chain in JET *J. Instrum.* **14** C11013
- [18] Štancar Ž. et al 2021 Experimental validation of an integrated modelling approach to neutron emission studies at JET *Nucl. Fusion* **61** 126030

- [19] Horton L. *et al* 1999 High fusion power steady state operation in JET DT plasmas *Nucl. Fusion* **39** 993–1008
- [20] Garzotti L. *et al* 2019 Scenario development for D–T operation at JET *Nucl. Fusion* **59** 076037
- [21] Garcia J. *et al* 2021 Integrated scenario development at JET for DT operation and ITER risk mitigation 28th IAEA Fusion Energy Conf. (Virtual event, 10–15 May) pp EX/1–2 (available at: https://conferences.iaea.org/event/214/papers/17020/files/6826-paper_v4_final.pdf)
- [22] Mailloux J. *et al* 2022 Overview of JET results for optimising ITER operation *Nucl. Fusion* **62** 042026
- [23] Maggi C.F. *et al* 2023 Overview of JET T and D-T results with Be/W wall *Nucl. Fusion* (submitted—29th FEC Special Issue)
- [24] Garcia J. *et al* 2022 New H-mode regimes with small ELMs and high thermal confinement in the Joint European Torus *Phys. Plasmas* **29** 032505
- [25] Garzotti L. *et al* 2023 Development of baseline scenario for high fusion performance at JET *Nucl. Fusion* (submitted)
- [26] Challis C. *et al* 2015 Improved confinement in JET high β plasmas with an ITER-like wall *Nucl. Fusion* **55** 053031
- [27] Challis C., Brezinsek S., Coffey I., Fontana M., Hawkes N.C., Keeling D.L., King D.B., Pucella G. and Viezzer E. 2020 Effect of fuel isotope mass on q-profile formation in JET hybrid plasmas *Nucl. Fusion* **60** 086008
- [28] Hobirk J. *et al* 2023 The JET hybrid scenario in D, T and D-T *Nucl. Fusion* **63** 112001
- [29] Maslov M. *et al* 2018 Observation of enhanced ion particle transport in mixed H/D isotope plasmas on JET *Nucl. Fusion* **58** 076022
- [30] Maslov M. *et al* 2023 JET D-T scenario with optimized non-thermal fusion *Nucl. Fusion* **63** 112002
- [31] Dumont R.J. *et al* 2018 Scenario development for the observation of alpha-driven instabilities in JET DT plasmas *Nucl. Fusion* **58** 082005
- [32] Fitzgerald M. *et al* 2023 Stability analysis of toroidal Alfvén eigenmodes observed in JET deuterium-tritium internal transport barrier plasmas *Nucl. Fusion* **63** 112006
- [33] Gallart D. *et al* 2022 Prediction of ICRF minority heating schemes for JET D–T experiments *Plasma Phys. Control. Fusion* **64** 125006
- [34] Lerche E. *et al* 2022 Fundamental ICRF heating of Deuterium ions in JET-DTE2 24th Topical Conf. on Radio-Frequency Power in Plasmas (Annapolis, Maryland, USA, 26–29 September) (available at: <https://pubs.aip.org/aip/acp/article/2984/1/030005/2907317>)
- [35] Mantsinen M. *et al* 2023 Experiments in high-performance JET plasmas in preparation of second harmonic ICRF heating of tritium in ITER *Nucl. Fusion* **63** 112015
- [36] Mantica P. *et al* 2023 Detection of alpha heating in JET-ILW D-T plasmas by a study of the electron temperature response to ICRH modulation *Nucl. Fusion* Private communication
- [37] Giroud C. *et al* 2023 Core-edge integrated neon-seeded scenario in deuterium- tritium at JET *Nucl. Fusion* Private communication
- [38] Giroud C. *et al* 2021 High performance ITER-baseline discharges in deuterium with nitrogen and neon-seeding in the JET-ILW 28th IAEA Fusion Energy Conf. (FEC 2020) (Virtual Event, 10–15 May) (available at: <https://nucleus.iaea.org/sites/fusionportal/Shared%20Documents/FEC%202020/fec2020-preprints/preprint0977.pdf>)
- [39] Pankin A., McCune D., Andre R., Bateman G. and Kritz A. 2004 The tokamak Monte Carlo fast ion module NUBEAM in the National Transport Code Collaboration library *Comput. Phys. Commun.* **159** 157–84
- [40] Brambilla M. 1999 Numerical simulation of ion cyclotron waves in tokamak plasmas *Plasma Phys. Control. Fusion* **41** 1–34
- [41] Grierson B.A. *et al* 2018 Orchestrating TRANSP simulations for interpretative and predictive tokamak modeling with OMFIT *Fusion Sci. Technol.* **74** 101–15
- [42] Meneghini O. *et al* 2015 Integrated modeling applications for tokamak experiments with OMFIT *Nucl. Fusion* **55** 083008
- [43] Kwon J.-M. *et al* 2006 Development of XGC-RF for global guiding-center particle simulation of minority ICRH heated plasmas in a general tokamak geometry *Bulletin of the American Physical Society, 48th Meeting of the Division of Plasma Physics (Philadelphia, 30 October–3 November)* (available at: <https://meetings.aps.org/Meeting/DPP06/Event/53184>)
- [44] Kwon J.-M., McCune D. and Chang C.S. 2007 Enhancement of NUBEAM for the simulation of fast ion and RF-wave interaction based on the quasi-linear theory *Bulletin of the American Physical Society, 49th Meeting of the Division of Plasma Physics (Orlando, USA, 12–16 November)* (available at: <https://meetings.aps.org/Meeting/DPP07/Event/71408>)
- [45] Kirov K. *et al* 2019 Fast ion synergistic effects in JET high performance pulses *Nucl. Fusion* **59** 056005
- [46] Frassinetti L., Beurskens M.N.A., Scannell R., Osborne T.H., Flanagan J., Kempenaars M., Maslov M., Pasqualotto R. and Walsh M. 2012 Spatial resolution of the JET Thomson scattering system *Rev. Sci. Instrum.* **83** 013506
- [47] Maslov M., Beurskens M.N.A., Kempenaars M. and Flanagan J. 2013 Status of the JET LIDAR Thomson scattering diagnostic *J. Instrum.* **8** C11009
- [48] Schmuck S., Fessey J., Gerbaud T., Alper B., Beurskens M.N.A., de la Luna E., Sirinelli A. and Zerbini M. 2012 Electron cyclotron emission measurements on JET: Michelson interferometer, new absolute calibration and determination of electron temperature *Rev. Sci. Instrum.* **83** 125101
- [49] Damm H. and Flanagan J. 2022 UKAEA Internal Report UK Atomic Energy Authority (available at: https://users.euro-fusion.org/expert/transp/Webpages/files/HRTS_calibration.pdf)
- [50] Hawkes N.C., Delabie E., Menmuir S., Giroud C., Meigs A.G., Conway N.J., Biewer T.M. and Hillis D.L. 2018 Instrumentation for the upgrade to the JET core charge-exchange spectrometers *Rev. Sci. Instrum.* **89** 10D113
- [51] Thorman A., Litherland-Smith E., Menmuir S., Hawkes N., O’Mullane M., Delabie E., Lomanowski B., Fontdecaba J.M. and Scully S. 2021 Visible spectroscopy of highly charged tungsten ions with the JET charge exchange diagnostic *Phys. Scr.* **96** 125631
- [52] Delabie E., Hawkes N., Biewer T.M. and O’Mullane M.G. 2016 *In situ* wavelength calibration of the edge CXS spectrometers on JET *Rev. Sci. Instrum.* **87** 11E525
- [53] Shumack A.E. *et al* 2014 x-ray crystal spectrometer upgrade for ITER-like wall experiments at JET *Rev. Sci. Instrum.* **85** 11E425
- [54] Weisen H., Delabie E., Flanagan J., Giroud C., Maslov M., Menmuir S., Patel A., Scott S., Siren P. and Varje J. 2020 Analysis of the inter-species power balance in JET plasmas *Nucl. Fusion* **60** 036004
- [55] Szepesti G. *et al* 2021 Advanced equilibrium reconstruction for JET with EFIT++ 47th EPS Plasma Physics Conf. (Stiges, Spain, 21–25 June) (available at: <http://ocs.ciemat.es/EPS2021PAP/pdf/P3.1037.pdf>)
- [56] von Hellermann M., Breger P., Frieling J., König R., Mandl W., Maas A. and Summers H.P. 1995 Analytical approximation of cross-section effects on charge exchange

- spectra observed in hot fusion plasmas *Plasma Phys. Control. Fusion* **37** 71–94
- [57] Vartanian S. *et al* 2021 Simultaneous H/D/T and 3He/4He absolute concentration measurements with an optical Penning gauge on JET *Fusion Eng. Des.* **170** 112511
- [58] Neverov V., Kukushkin A., Kruezi U., Stamp M.F. and Weisen H. 2019 Determination of isotope ratio in the divertor of JET-ILW by high-resolution H- α spectroscopy: H-D experiment and implications for D-T experiment *Nucl. Fusion* **59** 046011
- [59] Sertoli M., Carvalho P.J., Giroud C. and Menmuir S. 2019 Measuring the plasma composition in tokamaks with metallic plasma-facing components *J. Plasma Phys.* **85** 905850504
- [60] Casson F. *et al* 2020 Predictive multi-channel flux-driven modelling to optimise ICRH tungsten control and fusion performance in JET *Nucl. Fusion* **60** 066029
- [61] Köchl F. *et al* 2018 W transport and accumulation control in the termination phase of JET H-mode discharges and implications for ITER *Plasma Phys. Control. Fusion* **60** 074008
- [62] Boboc A., Gil C., Pastor P., Spuig P., Edlington T. and Dorling S. 2012 Upgrade of the JET far infrared interferometer diagnostic *Rev. Sci. Instrum.* **83** 10E341
- [63] Giannone L. *et al* 2021 Measurements and modelling of diamagnetic flux in ASDEX Upgrade *Nucl. Fusion* **61** 066021
- [64] Appelbe B. and Chittenden J. 2014 Relativistically correct DD and DT neutron spectra *High Energy Density Phys.* **11** 30–35
- [65] Goncharov P. 2015 Spectra of neutrons from a beam-driven fusion source *Nucl. Fusion* **55** 063012
- [66] Eriksson J., Conroy S., Andersson Sundén E. and Hellesen C. 2016 Calculating fusion neutron energy spectra from arbitrary reactant distributions *Comput. Phys. Commun.* **199** 40–46
- [67] Joffrin E. *et al* 2019 Overview of the JET preparation for deuterium–tritium operation with the ITER like-wall *Nucl. Fusion* **59** 112021
- [68] Garcia J. *et al* 2023 Modelling performed for predictions of fusion power in DTE2: overview and lessons learnt *Nucl. Fusion* **63** 112003
- [69] van Eester D. *et al* 2022 Maximising D-T fusion power by optimising the plasma composition and beam choice in JET *Plasma Phys. Control. Fusion* **64** 055014
- [70] Beurskens M.N.A. *et al* 2013 The effect of a metal wall on confinement in JET and ASDEX Upgrade *Plasma Phys. Control. Fusion* **55** 124043
- [71] Kim H.-T., Romanelli M., Voitsekhovitch I., Koskela T., Conboy J., Giroud C., Maddison G. and Joffrin E. 2015 Comparative analysis of core heat transport of JET high density H-mode plasmas in carbon wall and ITER-like wall *Plasma Phys. Control. Fusion* **57** 065002
- [72] Tegnered D., Strand P., Nordman H., Giroud C., Kim H.-T., Maddison G.P., Romanelli M. and Szepesi G. 2016 Comparative gyrokinetic analysis of JET baseline H-mode core plasmas with carbon wall and ITER-like wall *Plasma Phys. Control. Fusion* **58** 045021
- [73] Budny R. and Cordey J. 2016 Core fusion power gain and alpha heating in JET, TFTR and ITER *Nucl. Fusion* **56** 056002
- [74] Kim H.-T., Sips A., Romanelli M., Challis C.D., Rimini F., Garzotti L., Lerche E., Buchanan J., Yuan X. and Kaye S. 2018 High fusion performance at high T_i/T_e in JET-ILW baseline plasmas with high NBI heating power and low gas puffing *Nucl. Fusion* **58** 036020
- [75] Siren P. *et al* 2019 Comprehensive benchmark studies of ASCOT and TRANSP-NUBEAM fast particle simulations *46th EPS Plasma Physics Conf. (Milan, Italy, 8–12 July)* p P4.1026 (available at: <http://ocs.ciemat.es/EPS2019PAP/pdf/P4.1026.pdf>)
- [76] Kirov K.K. *et al* 2022 Impact of ICRH heating of fast D and T ions on fusion performance in JET DTE2 campaign *24th Topical Conf. on Radio-Frequency Power in Plasmas (Annapolis, Maryland, USA, 26–28 September)* (available at: <https://pubs.aip.org/aip/acp/article/2984/1/040001/2907331/Impact-of-ICRH-heating-of-fast-D-and-T-ions-on>)
- [77] Kazakov Y.O. *et al* 2021 Physics and applications of three-ion ICRF scenarios for fusion research *Phys. Plasmas* **28** 020501
- [78] Gallart D. *et al* 2018 Modelling of JET hybrid plasmas with emphasis on performance of combined ICRF and NBI heating *Nucl. Fusion* **58** 106037
- [79] Kirov K.K. *et al* 2023 Impact of RF waves—fast NBI ions interaction on the fusion performance in JET DTE2 campaign *Nucl. Fusion* (submitted)
- [80] van Eester D. *et al* 2022 RF power as key contributor to high performance “baseline” scenario experiments in JET DD and DT plasmas in preparation for ITER *24th Topical Conf. on Radio-Frequency Power in Plasmas (Annapolis, Maryland, USA, 26–28 September)* (available at: <https://pubs.aip.org/aip/acp/article/2984/1/030004/2907316/RF-power-as-key-contributor-to-high-performance>)
- [81] King D.B. *et al* 2023 Tritium neutral beam injection on JET: calibration and plasma measurements *Nucl. Fusion* **63** 112005
- [82] Jones O.M. *et al* 2015 Measurements and modelling of fast-ion redistribution due to resonant MHD instabilities in MAST *Plasma Phys. Control. Fusion* **57** 125009
- [83] Weiland M., Bilato R., Collins C., Heidbrink W.W., Liu D. and Van Zeeland M.A. 2019 Simulation of neutron emission in neutral beam injection heated plasmas with the real-time code RABBIT *Nucl. Fusion* **59** 086002
- [84] Thome K.E. 2022 Influence of energetic particle profiles on DIII-D high bootstrap fraction plasmas *64th Annual Meeting of the APS Division of Plasma Physics (Spokane, Washington, USA, 17–21 October)* (American Physical Society) (available at: <https://meetings.aps.org/Meeting/DPP22/Session/BI01.5>)
- [85] Tardini G., Höhbauer C., Fischer R. and Neu R. 2013 Simulation of the neutron rate in ASDEX Upgrade H-mode discharges *Nucl. Fusion* **53** 063027
- [86] Teplukhina A.A. *et al* (JET Contributors) 2021 Fast ion transport by sawtooth instability in the presence of ICRF-NBI synergy in JET plasmas *Nucl. Fusion* **61** 116056
- [87] Bosch H.-S. and Hale G.M. 1992 Improved formulas for fusion cross-section and thermal reactivities *Nucl. Fusion* **32** 611–31
- [88] Akers R.J. *et al* 2012 GPGPU Monte Carlo calculation of gyro-phase resolved fast ion and n-state resolved neutral deuterium distributions *39th EPS Conf. and 16th Int. Congress on Plasma Physics (Stockholm, Sweden, 2–6 July)* p P5.088 (available at: <http://ocs.ciemat.es/epsicpp2012pap/pdf/P5.088.pdf>)
- [89] Fitzgerald M., Buchanan J., Akers R., Breizman B.N. and Sharapov S.E. 2020 HALO: a full-orbit model of nonlinear interaction of fast particles with eigenmodes *Comput. Phys. Commun.* **252** 106773
- [90] Ceconello M. *et al* 2019 Analysis of TAEs and FBs induced fast ions redistribution and losses in MAST using a reduced fast ion transport model *16th IAEA Technical Meeting on Energetic Particles in Magnetic Confinement Systems—Theory of Plasma Instabilities (Shizuoka, Japan,*

- 3–6 September) (available at: <https://conferences.iaea.org/event/185/contributions/15029/contribution.pdf>)
- [91] Heidbrink W. *et al* 2018 The phase-space dependence of fast-ion interaction with tearing modes *Nucl. Fusion* **58** 082027
- [92] Jarvis O.N., Clipsham E.W., Hone M.A., Laundry B.J., Pillon M., Rapisarda M., Sadler G.J., van Belle P. and Verschuur K.A. 1991 Use of activation technique for the measurement of neutron yields from deuterium plasmas at the Joint European Torus *Fusion Technol.* **20** 265–84
- [93] Bourdelle C., Camenen Y., Citrin J., Marin M., Casson F.J., Koechl F. and Maslov M. 2018 Fast H isotope and impurity mixing in ion-temperature-gradient turbulence *Nucl. Fusion* **58** 076028
- [94] Marin M., Citrin J., Bourdelle C., Camenen Y., Casson F.J., Ho A., Koechl F. and Maslov M. 2020 First-principles-based multiple-isotope particle transport modelling at JET *Nucl. Fusion* **60** 046007
- [95] Hammett G. 1986 Fast ion studies of ion cyclotron heating in the PLT tokamak *PhD Dissertation* No. GAX86-12694 University Microfilms International, Princeton
- [96] Mazzi S. *et al* (JET Contributors) 2022 Enhanced performance in fusion plasmas through turbulence suppression by megaelectronvolt ions *Nat. Phys.* **18** 776–82
- [97] Bierwage A. *et al* 2022 Energy-selective confinement of fusion-born alpha particles during internal relaxations in a tokamak plasma *Nat. Commun.* **13** 3941
- [98] Žohar A. *et al* (JET Contributors) 2022 Validation of realistic Monte Carlo plasma gamma-ray source on JET discharges *Nucl. Fusion* **62** 066004
- [99] Bonfigli P.J. *et al* 2022 Lost alpha Faraday cup foil noise characterization during Joint European Torus plasma post-processing analysis *Rev. Sci. Instrum.* **93** 093527
- [100] Järleblad H., Stagner L., Salewski M., Eriksson J., Nocente M., Rasmussen J., Štancar Ž., Kazakov Y.O. and Simmendefeldt B. (JET Contributors) 2022 Fast-ion orbit sensitivity of neutron and gamma-ray diagnostics for one-step fusion reactions *Nucl. Fusion* **62** 112005
- [101] Trkov A. *et al* 2020 IRDFF-II: a new neutron metrology library *Nucl. Data Sheets* **163** 1–108
- [102] Hirvijoki E., Asunta O., Koskela T., Kurki-Suonio T., Miettunen J., Sipilä S., Snicker A. and Äkäslompolo S. 2014 ASCOT: solving the kinetic equation of minority particle species in tokamak plasmas *Comput. Phys. Commun.* **185** 1310–21
- [103] Kiptily V. *et al* 2023 Evidence of electron heating by alpha particles in JET deuterium-tritium plasmas *Phys. Rev. Lett.* **131** 075101
- [104] Sharapov S.E. *et al* 2023 Excitation of AEs by alpha-particles with bump-on tail distribution in JET *Nucl. Fusion* **63** 112007
- [105] Oliver H.J.C. *et al* 2023 Toroidal Alfvén eigenmodes observed in low power JET deuterium–tritium plasmas *Nucl. Fusion* **63** 112008
- [106] Petrov Y.V. and Harvey R.W. 2016 A fully-neoclassical finite-orbit-width version of the CQL3D Fokker–Planck code *Plasma Phys. Control. Fusion* **58** 115001
- [107] Kazakov Y.O., Ongena J., Eester D.V., Bilato R., Dumont R., Lerche E., Mantsinen M. and Messiaen A. 2015 A new ion cyclotron range of frequency scenario for bulk ion heating in deuterium-tritium plasmas: how to utilize intrinsic impurities in our favour *Phys. Plasmas* **22** 082511